energies

MDPI

Article

Robust Power Sharing and Voltage Stabilization Control Structure via Sliding-Mode Technique in Islanded Micro-Grid

Quan-Quan Zhang and Rong-Jong Wai *

Department of Electronic and Computer Engineering, National Taiwan University of Science and Technology, Taipei 106, Taiwan; hizhangqq@163.com

* Correspondence: rjwai@mail.ntust.edu.tw; Tel.: +886-2-27376367

Abstract: With a focus on the problems of active power sharing and voltage deviation of parallel-connected inverters in an islanded micro-grid (MG), in this study, the power-voltage droop controller and the inner voltage regulator are redesigned based on a total sliding-mode control (TSMC) technique. As for the power-voltage droop control loop, a droop control relation error between the active power and the point-of-common-coupling (PCC) voltage amplitude is defined. Then, the TSMC scheme is adopted to reach the new droop control relation, where the active power sharing and voltage amplitude recovery can be achieved simultaneously. Owing to the faster dynamic response and strong robustness provided by the TSMC framework, high-precision active power sharing during transient state also can be ensured without the influence of line impedances. The power allocation error can be improved by more than 81.2% and 50% than the conventional and proportional-integral (PI)-based droop control methods, respectively, and the voltage deviation rate can be reduced to 0.16%. Moreover, a small-signal model of the TSMC-based droop-controlled system is established, and the influences of control parameters on the system stability and the dynamic response are also investigated. The effectiveness of the proposed control method is verified by numerical simulations and experimental results.

Keywords: droop control; micro-grid; voltage stabilization; power sharing; total sliding-mode control (TSMC)

Citation: Zhang, Q.-Q.; Wai, R.-J. Robust Power Sharing and Voltage Stabilization Control Structure via Sliding-Mode Technique in Islanded Micro-Grid. *Energies* **2021**, *14*, 883. https://doi.org/10.3390/en14040883

Academic Editor: Roberto Sacile
Received: 15 January 2021
Accepted: 4 February 2021
Published: 8 February 2021

1. Introduction

As with the control technology for parallel-connected inverters, the droop control has been widely used in the micro-grid (MG) [1–4]. Especially for the islanded operation mode, the droop control can maintain the voltage amplitude/frequency stability and adjust the power allocation proportion among multiple inverters simultaneously [5]. For a MG with a medium or low voltage, the system impedance generally exhibits a complex impedance characteristic. As a result, the coupling always exists between active and reactive power control, which will weaken the system control performance. Therefore, the virtual impedance with different components is often introduced to change the impedance characteristics of the system [6–8]. However, the virtual impedance method may bring about a voltage drop on the voltage reference, which will deteriorate the voltage quality, and make the voltage more sensitive to the change of load currents.

For each parallel-connected inverter, the control structure can be divided into two parts, which are the outer power droop control loop and the inner voltage control loop. The power droop control will cause steady-state voltage amplitude and frequency deviations, which is one of its shortcomings. In addition, for the conventional active power-frequency/reactive power-voltage (*P-f*/*Q-U*) droop control, the accurate reactive power sharing is difficult to be ensured, and the control performance is affected by hardware parameters [9]. Recently, various droop-control-based methods have been concentrated on solving the issues of poor reactive power sharing or voltage and frequency deviations.

Pogaku et al. [10] tried to reduce reactive power sharing error by increasing droop coefficients. However, the practical effectiveness is restricted when large line impedances exist, and the selection of droop coefficients to be large may cause the system instability. Guerrero et al. [11], Wang et al. [12] and Guan et al. [13] have introduced several virtual-impedance-based methods, which can compensate for the mismatch of the system impedance. The methods in [11–13] are simple and effective for power sharing when a large virtual impedance is adopted. Nevertheless, a large virtual impedance may result in a huge voltage drop, and the voltage quality will be deteriorated. Similarly, for an active power-voltage/reactive power-frequency (*P-U*/*Q-f*) droop-controlled system, the accurate reactive power sharing can be achieved, but the high-precision active power sharing is difficult to be ensured. In order to achieve accurate active power sharing among parallel-connected inverters, Zhong et al. [14] and Wai et al. [15] focused on designing integral-based and proportional-integral (PI)-based *P-U* droop control structures, respectively. By using a feedback loop of the common AC-bus voltage, the load voltage derivation also can be reduced. These methods in [14,15] are effective for active power sharing and load voltage restoration. However, the adding of the integral behavior on the proportional droop controller will degrade the dynamic response. Besides, the transient power sharing performance is a latent problem to be solved.

Kahrobaeian and Mohamed [16] proposed a networked-based distributed power sharing control structure for islanded microgrid systems, which can provide the system with accurate active and reactive power sharing and eliminate the frequency deviations. As for this method in [16], the power measurements of parallel inverters are transmitted to a centralized energy management unit (EMU) for calculating the share of each unit of the total power demand based on pre-defined optimization criteria. Then, the optimized set points are sent to each distributed power regulators to realize the optimized power generation. Because the feedback power signals are adopted from the local measurements, and only power reference values are affected by communication delays, the system with the proposed method in [16] shows great robustness against communication delays. However, due to the compensation term added on the command voltage magnitude, the voltage deviation cannot be avoided. Besides, the point-of-common-coupling (PCC) voltage may further drop due to the transmission line impedance, which will bring more challenges to the grid connection process. Mahmud et al. [17] presented a coordinated multilayer control strategy for the energy management of grid-connected ac micro-grids. The coordination control is performed between the tertiary energy management layer and the primary control layer. In the tertiary layer, the autoregressive-moving-average-based and the artificial-neural-network-based techniques are used to predict the customer's power demand and the photovoltaics power generations. The day-ahead precautionary measures are implemented to tackle uncertainties. Then, the reference power generated by the tertiary energy management layer is sent to each inverter for the power regulation. The day-ahead prediction and management significantly reduce the peak power demand and uncertainties during actual operation.

With a focus on improving the voltage quality, Shan et al. [18] investigated a comprehensive method integrated of a model predictive power control scheme for bidirectional dc–dc converters, a model predictive control (MPC) scheme for the inverter voltage, and a washout-filter-based power sharing strategy. In order to restore the PCC voltage amplitude, the voltage drop across the transmission line impedance is estimated and added on the voltage amplitude command. This method is effective for mitigating the voltage and frequency deviations, and the AC voltage quality can be improved by the model predictive voltage control scheme. However, the power sharing performance may be deteriorated when the line impedances of parallel inverters differ from each other. Besides, the impedance evaluate methods are required to obtain the exact information of line impedances, which complicates the control system and reduces the system robustness to line impedance variations. Zhu et al. [19] designed an accurate power sharing strategy with a control center. The compensation signals to be calculated by a central controller are sent to each inverter via

transmission lines. Then, reactive power references can be tuned to enhance the property of reactive power sharing. However, it suffers from the problem of "single point of failure" for the central control unit, which may deteriorate the system reliability and scalability. Similarly, a pinning-based hierarchical and distributed cooperative control strategy has been presented in [20], which can achieve frequency restoration and an accurate reactive power sharing among distributed-generation (DG) units. Moreover, an economic operation of the system by minimizing the overall generation cost has been covered in [20]. However, the tradeoff between power sharing and voltage restoration is an admittedly problem to be solved. A washout-filter-based method has been initially studied in [21] for the aim of improving the load voltage quality without communication lines. Unfortunately, it has not covered the reactive power sharing performance, and the system robustness to line impedance and dynamic behavior in [21] should be further explored. The major contributions and drawbacks of the corresponding researches in [11–21] are summarized in Table 1. The motivation of this study is to design a non-linear robust control strategy for reducing the contradictory between the power sharing and the PCC voltage deviation, realizing the power sharing in both steady and transient states, improving the system dynamic response and enhancing the system robustness to uncertainties (e.g., line impedances).

Table 1. Research comparisons of different control methods.

Control Methods	Main Contributions	Drawbacks
Virtual-impedance-based method [11–13]	Improve power sharing performance Easy to implement	Increase the voltage drop Poor robustness
PI-based droop control [14,15]	Accurate power sharing and voltage restoration Robust to line impedance	Dynamic performance to be further improved
Centralized control [1,19]	Simple structure Accurate power sharing Voltage and frequency restoration	Suffer from the problem of "single point of failure" for central control unit
Hierarchical control [16,17,20]	Accurate power sharing Voltage and frequency restoration Optimized power generation	Tradeoff between power sharing and voltage restoration
Washout-filter-based method [18,21]	Mitigate voltage and frequency deviation Communication-free	Poor robustness to line impedance Dynamic performance to be further improved

As one of the effective nonlinear robust control strategies, sliding-mode control (SMC) has received considerable attention in recent years [22–24]. It can provide the system with fast transient response and strong robustness against parameter variations and disturbances once the system dynamics are controlled in the sliding mode [25,26]. Morales et al. [27] presented a control strategy for a three-phase shunt active power filters (SAPFs), which was designed using the SMC with the vector operation technique (VOT). In [27], the objectives of the good current tracking ability and the reduction of the switching losses can be achieved. Guzman et al. [28] proposed a sliding-mode observer-based controller, which used a reduced state-space model without relying on the grid inductance value. No self-tuning procedures or adaptive techniques were required, and a strong robustness against uncertainties was also ensured in [28]. Note that, the sliding surfaces in [27,28] only contain the controlled error variable to be suitable for first-order dynamic systems, unsuitable for second-order and above dynamic systems. Vieira et al. [29] expressed a multi-loop control strategy for a grid-connected voltage source inverter (VSI). The inner loop was implemented by a discrete-time SMC scheme to realize the tracking of the converter-side current. Different from [27,28], the design of the control effort including an extra sliding-surface term in [29] can effectively alleviate the chattering phenomena caused by the sign function. Mokhtar et al. [30] presented an adaptive droop scheme for a dc micro-grid, and a multivariable SMC was adopted in the inner loop to simultaneously manipulate the output voltage and the input current. Similarly, in [31], a multivariable sliding surface is adopted for the capacitor voltage control of a three-phase grid-tied LCL-filtered VSI. Delghavi and Yazdani [32] investigated a current-controlled voltage-mode control scheme based

on a multivariable SMC strategy in a master-slave organized micro-grid. Although the application of the multivariable sliding surfaces in [30–32] can simplify the design process of the control system and improve the control precision of a high-order dynamic system, more sensors with high cost are inevitable. In order to keep the robustness during the whole SMC system, a total SMC (TSMC) strategy was designed in [33,34] for the voltage and current tracking control of dc-ac inverters. The control strategies in [33,34] assured a sliding motion through the entire state trajectory. Therefore, the controlled system is robust to uncertainties through the whole control process.

In this study, a TSMC-based droop control structure including an outer *P-U*/*Q-f* droop control loop and an inner voltage control loop is investigated for parallel-connected inverters in an islanded MG. The sliding surfaces for the TSMC-based droop controller and the TSMC-based voltage controller are designed via the proportional-integral (PI) type and the proportion-integration-differentiation (PID) type, respectively. The major contribution of the proposed control scheme in this study can be summarized as follows.

(i) More accurate active power sharing during both the transient and steady states can be ensured, and smaller voltage amplitude deviation can be achieved due to the proposed TSMC-based *P-U* droop control scheme. Moreover, the active power sharing and the voltage amplitude are insensitive to system hardware parameters.
(ii) Strong robustness and better voltage tracking property can be obtained due to the PID-type TSMC scheme for the inner capacitance-voltage control.
(iii) The TSMC-based frameworks for both the inner voltage loop and the droop control loop endow the system with the performances of fast dynamic response, high control precision and strong robustness to uncertainties.
(iv) The small-signal model of the TSMC-based droop-controlled system gives detailed analyses of the parameter influence on the system stability and the dynamic responses.

This study is mainly organized into six sections. Following the introduction, the basic description of the *P-U*/*Q-f* droop control method is conducted in Section 2. In Section 3, a novel TSMC-based *P-U*/*Q-f* droop control method is designed, and the capacitance-voltage control based on TSMC is described in detail. In Section 4, parameter influences on the system stability and the dynamic response of the TSMC-based droop-controller are investigated based on small-signal stability analyses. In Section 5, numerical simulations and experimental results are performed to demonstrate the effectiveness and robustness of the proposed control scheme in comparisons with other existing control frameworks. Finally, some conclusions are drawn in Section 6.

2. Basic Description of Droop Control Method

Figure 1 shows the simplified structure of an islanded micro-grid (MG), in which the loads are shared between parallel-connected distributed generations (DGs) though power transmission lines (PTL). In Figure 1, an inverter is involved for each DG to convert a direct current into an alternating current, and then a three-phase LC filter is added for a high-quality voltage.

The conventional droop control is designed based on a purely resistive or inductive system impedance, where the power coupling does not exist [2]. Note that, a purely resistive or inductive system impedance is the ideal case, not for the actual system in practical applications. Thus, a virtual complex impedance is always introduced to eliminate the power coupling [15]. Assuming that the phase angle difference between the DG port voltage and the point-of-common-coupling (PCC) voltage is small enough to be neglected, then according to the power flow characteristic [15], the output active and reactive power of the inverter n can be expressed as

$$\begin{bmatrix} P_n \\ Q_n \end{bmatrix} = \begin{bmatrix} \frac{3X_nU_nE}{2(R_n^2+X_n^2)} & \frac{3R_nU_n}{2(R_n^2+X_n^2)} \\ -\frac{3R_nU_nE}{2(R_n^2+X_n^2)} & \frac{3X_nU_n}{2(R_n^2+X_n^2)} \end{bmatrix} \begin{bmatrix} \Delta\delta_n \\ \Delta U_n \end{bmatrix}. \quad (1)$$

When the line impedance is purely resistive, (1) can be approximately represented as

$$\begin{bmatrix} P_n \\ Q_n \end{bmatrix} = \begin{bmatrix} 0 & \frac{3U_n}{2R_n} \\ -\frac{3U_nE}{2R_n} & 0 \end{bmatrix} \begin{bmatrix} \Delta\delta_n \\ \Delta U_n \end{bmatrix} = \begin{bmatrix} 0 & k_{\mathrm{pu}} \\ k_{q\delta} & 0 \end{bmatrix} \begin{bmatrix} \Delta\delta_n \\ \Delta U_n \end{bmatrix}, \tag{2}$$

where R_n represents the line resistance; U_n is the output capacitance-voltage amplitude of the nth inverter; E is the voltage amplitude of the point of common coupling (PCC); k_{pu} and $k_{q\delta}$ are the correlation coefficients; k_{pu} is defined as $3U_n/(2R_n)$, and $k_{q\delta}$ is defined as $-3U_nE/(2R_n)$.

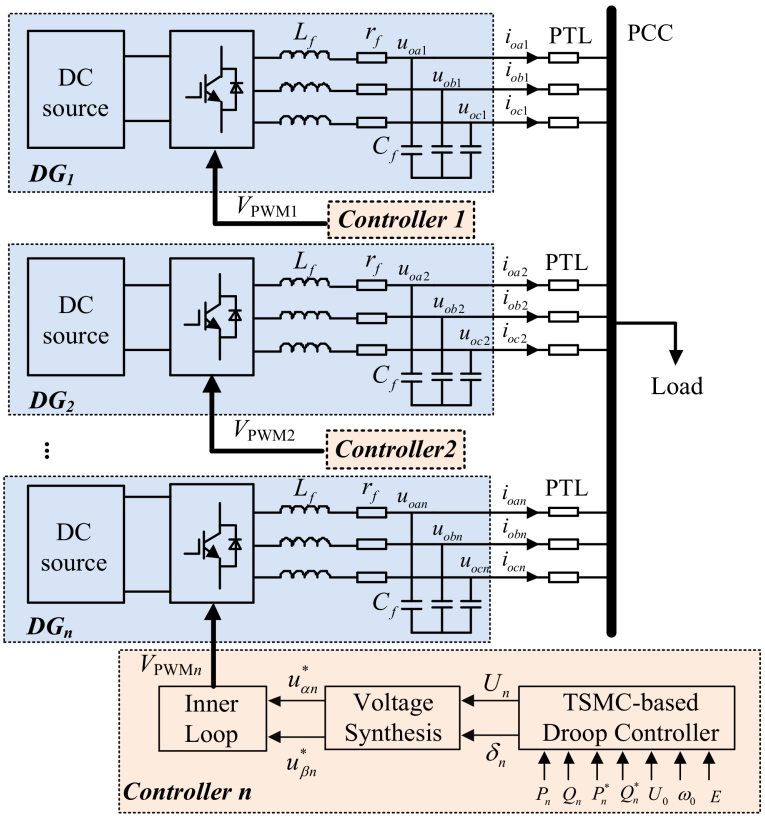

Figure 1. Simplified structure of islanded micro-grid.

For the system with resistive impedance, the *P-U* droop control loop can adjust the output active power (P_n) and provide the system with a voltage command (U_n), the *Q-f* droop control loop can adjust the output reactive power (Q_n) and provide the system with a frequency command (ω_n). Therefore, the corresponding droop control formula can be expressed as

$$\begin{cases} U_n - U_0 = -m_n(P_n - P_n^*) \\ \omega_n - \omega_0 = n_n(Q_n - Q_n^*) \end{cases}, \tag{3}$$

where U_0 and ω_0 are the rated voltage amplitude and the rated angular frequency, respectively; P_n^* and Q_n^* represent rated active and reactive powers, respectively. m_n and n_n are droop coefficients to be set in inverse proportion to the rated active and reactive powers (P_n^* and Q_n^*), respectively. Note that, the relations of $m_1P_1^* = m_2P_2^* = \cdots = m_nP_n^*$ and $n_1Q_1^* = n_2Q_2^* = \cdots = n_nQ_n^*$ always exist.

As can be seen from (3), the voltage amplitude and frequency commands generated by the conventional droop control always suffer from steady-state deviations. Besides, the deviation may be further increased by the voltage drop due to the virtual impedance. Actually, the reactive power can be shared accurately between the parallel inverters through the *Q-f* droop control loop, but the high-precision active power sharing is a latent problem to be solved. Note that, every power (active or reactive) to be related to the frequency in

the droop equation will have accurate power sharing because frequencies of inverters will reach the same amounts at the steady state. However, it is not the same case by the voltage amplitude, and the system will suffer from inaccurate power sharing when the power is related to the voltage amplitude in the droop equation.

Inspired by the reactive power sharing mechanism of the *Q-f* droop control loop, Zhong et al. [14] and Wai et al. [15] tried to introduce an integral-based controller and a proportional-integral (PI)-based controller, respectively, together with a voltage feedback structure for the active power control loop. These methods in [14,15] are effective for achieving the accurate active power sharing and reducing the voltage derivation. However, affected by the integral behavior added on the proportional droop controller, the dynamic performance is degraded. Besides, the transient power sharing performance is still affected by hardware parameters. By focusing on the problems mentioned above, the *P-U* droop controller and the inner voltage regulator will be redesigned based on a total sliding-mode control (TSMC) method in this study. The TSMC-based scheme to be designed for both the droop control loop and the inner voltage loop can provide the system with the performances of high control precision, fast dynamic response and strong robustness. As for the droop controller design, the droop relationship between the active power and the PCC voltage amplitude is taken as the final target, where the PCC voltage amplitude is a global signal. Then, the TSMC scheme is adopted to obtain the equation between the active power and the PCC voltage amplitude. Compared with the PI-based droop control method in [15], the proposed TSMC-based droop controller can provide the system with better dynamics and stronger robustness against uncertainty changes and line impedance.

3. Proposed TSMC-Based Power and Voltage Control Structure

Figure 2 shows the overall control structure of the system. It combines a TSMC-based droop controller to be designed in Section 3.1, a virtual complex impedance part and a total sliding-mode voltage controller to be designed in Section 3.2. Firstly, the TSMC-based droop controller is designed to achieve accurate active power sharing and enhance the voltage stabilization, and the detailed design procedure is introduced as follows.

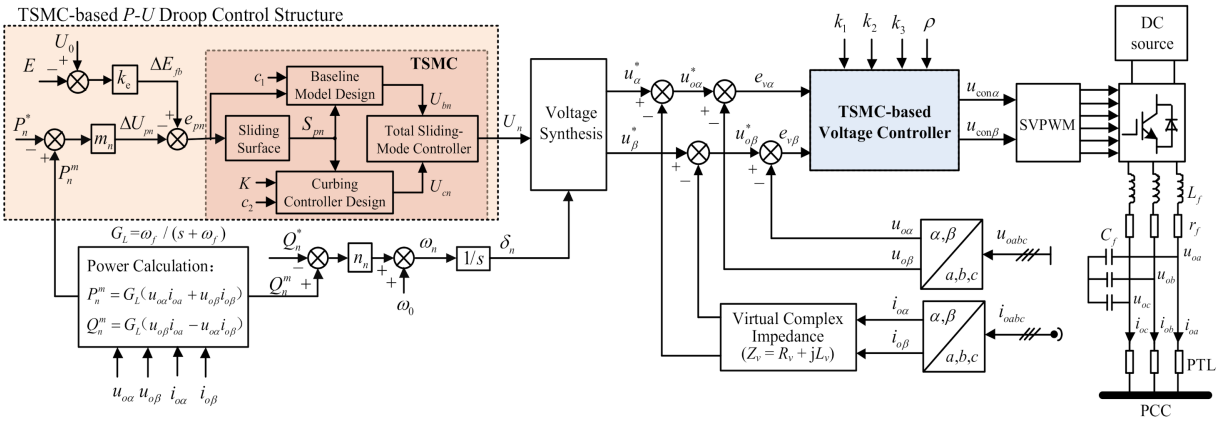

Figure 2. Diagram of proposed control structure.

3.1. TSMC-Based P-U Droop Control Scheme

Due to the influence of the low-pass power filter, the dynamics of the inner voltage control loop and the *LC* filter are much faster than that of the droop control module. Therefore, when considering the dynamic of the power control loop, the influence of the inner faster dynamic blocks can be neglected. According to the first row of (2) and the relation of $\Delta U_n = U_n - E$, the output active power of the three-phase inverter can be derived as

$$P_n = k_{\mathrm{pu}}(U_n - E). \tag{4}$$

The measured value of the output active power (P_n^m) can be obtained through a low-pass filter and is derived as

$$\dot{P}_n^m = -\omega_f P_n^m + \omega_f P_n, \tag{5}$$

where ω_f denotes the cutoff frequency of the low-pass power filter.

By substituting (4) to (5), it yields

$$\dot{P}_n^m = -\omega_f P_n^m + \omega_f k_{\mathrm{pu}}(U_n - E) = -\omega_f P_n^m + \omega_f \left(k_{\mathrm{pun}} + \Delta k_{\mathrm{pu}}\right)(U_n - E) = -\omega_f P_n^m + \omega_f k_{\mathrm{pun}}(U_n - E) + D_{\mathrm{pn}}, \tag{6}$$

where $k_{pu} = k_{pun} + \Delta k_{pu}$, in which k_{pun} is the nominal value of k_{pu} and Δk_{pu} represents the system parameter variation; $D_{pn} = \omega_f \Delta k_{pu}(U_n - E)$ represents the uncertainty component caused by parameter variations (Δk_{pu}). As for the active power-voltage droop control loop, the uncertainty of the line impedance is considered. The uncertainty component caused by line impedance variations can be derived from (6) and represented as

$$D_{pn} = \omega_f \Delta k_{pu}(U_n - E) = \frac{3\Delta R_n \omega_f U_n (U_n - E)}{2R_{n0}(R_{n0} + \Delta R_n)}, \tag{7}$$

where R_{n0} denotes the nominal value of the line resistance (R_n); ΔR_{n0} represents the variation of the line resistance. The bound of D_{pn} is assumed to be $|D_{pn}| < K$, where $|\cdot|$ is the operator of an absolute value, and K is a given positive constant.

In order to ensure an accurate active power sharing while improving the PCC voltage quality, a droop control relation error (e_{pn}) is defined as

$$e_{\mathrm{pn}} = \Delta E_{\mathrm{fb}} - \Delta U_{\mathrm{pn}} = k_e(U_0 - E) - m_n(P_n^m - P_n^*), \tag{8}$$

where $\Delta E_{fb} = k_e(U_0 - E)$ is the feedback term of the PCC voltage deviation, in which k_e is the proportional factor of the U_0-E feedback loop; $\Delta U_{pn} = m_n(P_n^m - P_n^*)$ is the proportional term of the active power deviation. A TSMC-based scheme is adopted to force the term of e_{pn} to be zero and reach a novel droop control formula as (9).

$$E = U_0 - \frac{m_n(P_n^m - P_n^*)}{k_e} \tag{9}$$

The derivative of the droop control relation error ($\dot{e}_{\mathrm{pn}}(t)$) can be derived from (6) and (8) as

$$\dot{e}_{\mathrm{pn}}(t) = \Delta\, \dot{E}_{\mathrm{fb}} - \Delta\, \dot{U}_{\mathrm{pn}} = -k_e\, \dot{E} - m_n\, \dot{P}_n^m = -k_e\, \dot{E} - m_n\left[-\omega_f P_n^m + \omega_f k_{\mathrm{pun}}(U_n - E) + D_{\mathrm{pn}}\right]. \tag{10}$$

Define a proportional-integral (PI)-type total sliding surface as

$$S_{\mathrm{pn}}(t) = e_{\mathrm{pn}}(t) + c_1 \int_0^t e_{\mathrm{pn}}(\tau) d\tau - e_{\mathrm{pn}}(0), \tag{11}$$

where $e_{pn}(0)$ is the initial value of $e_{pn}(t)$; c_1 is given a positive constant.

By making $\dot{S}_{\mathrm{pn}}(t) = 0$ and substituting (10), the baseline model control law without parameter uncertainties ($D_{pn} = 0$) can be designed as

$$U_{\mathrm{bn}} = \frac{1}{m_n \omega_f k_{\mathrm{pun}}}\left(m_n \omega_f P_n^m + m_n \omega_f k_{\mathrm{pun}} E - k_e\, \dot{E} + c_1 e_{\mathrm{pn}}\right). \tag{12}$$

When the system is subjected to unknown parameter variations and external disturbances, the control law in (12) cannot ensure that (6) satisfies the baseline model performance and $\dot{S}_{\mathrm{pn}}(t) = 0$ for $t > 0$. In order to make the closed-loop error dynamic of the

controlled system as the same as the performance in the baseline model design, an auxiliary control law (U_{cn}) is necessary. Therefore, the final control law can be designed as

$$U_n = U_{\mathrm{bn}} + U_{\mathrm{cn}}, \tag{13}$$

where U_{bn} is the same as (12). By substituting (13) into (6), the system error dynamic model becomes

$$\dot{S}_{\mathrm{pn}}(t) = \dot{e}_{\mathrm{pn}}(t) + c_1 e_{\mathrm{pn}}(t) = -m_n \omega_f k_{\mathrm{pun}} U_{\mathrm{cn}} - D_{\mathrm{pn}}(t). \tag{14}$$

Define a Lyapunov function as

$$V_P = \frac{1}{2} S_{\mathrm{pn}}^2(t). \tag{15}$$

By differentiating V_p and combining (12), one can obtain

$$\dot{V}_P = S_{\mathrm{pn}}(t)\, \dot{S}_{\mathrm{pn}}(t) = -S_{\mathrm{pn}}(t)\left[m_n \omega_f k_{\mathrm{pun}} U_{\mathrm{cn}} + D_{\mathrm{pn}}(t)\right]. \tag{16}$$

To make $\dot{V}_P$ to be a negative-definite function, U_{cn} can be designed as

$$U_{\mathrm{cn}} = \frac{K}{m_n \omega_f k_{\mathrm{pun}}} \mathrm{sgn}(S_{\mathrm{pn}}(t)) + \frac{c_2}{m_n \omega_f k_{\mathrm{pun}}} S_{\mathrm{pn}}(t), \tag{17}$$

where sgn(·) is the sign function, and c_2 is a given positive constant. Note that, the second term of U_{cn} is helpful to reduce the chattering phenomena in the control signal (U_n). By substituting (17) to (16), it yields

$$\begin{aligned} \dot{V}_P &= S_{\mathrm{pn}}(t)\, \dot{S}_{\mathrm{pn}}(t) = -S_{\mathrm{pn}}\Big(t)[m_n \omega_f k_{\mathrm{pun}} U_{\mathrm{cn}} + D_{\mathrm{pn}}\Big(t)] = -c_2 S_{\mathrm{pn}}^2(t) - K\big|S_{\mathrm{pn}}(t)\big| - S_{\mathrm{pn}}(t) D_{\mathrm{pn}}(t) \\ &\le -c_2 S_{\mathrm{pn}}^2(t) - K\big|S_{\mathrm{pn}}(t)\big| + \big|S_{\mathrm{pn}}(t)\big|\big|D_{\mathrm{pn}}(t)\big| = -c_2 S_{\mathrm{pn}}^2(t) - \big|S_{\mathrm{pn}}(t)\big|\Big[K - \big|D_{\mathrm{pn}}(t)\big|\Big] < -c_2 S_{\mathrm{pn}}^2(t) < 0. \end{aligned} \tag{18}$$

As can be seen from (18), the asymptotic stability of the TSMC-based power control loop can be guaranteed without the influence of system uncertainties, and the sliding motion can be assured during the whole control period. Therefore, superior dynamic performance can be assured, and the error of state variables will converge exponentially to zero once the system state trajectory reaches the sliding surface [24]. The chattering phenomena caused by the sign function can be alleviated by an additional sliding-surface term ($c_2 S_{pn}(t)/(m_n \omega_f k_{pun})$) in the curbing control law in (17). As can be seen in (18), the term $-c_2 S_{\mathrm{pn}}^2(t)$ can dominate the fact of $\dot{V}_P < 0$ even the worst cased $|D_{pn}| > K$ happens, which means that the parameter K could be conservatively selected to avoid increasing the chattering phenomena caused by the sign-function term of $K\mathrm{sgn}(S_{pn}(t))/(m_n \omega_f k_{pun})$.

Since the droop control relation error (e_{pn}) in (8) can be controlled to be zero by the control law in (13), the novel droop control formula (9) can be reached. Then, the following relation can be derived from (9):

$$m_1(P_1^m - P_1^*) = m_2(P_2^m - P_2^*) = \cdots = m_n(P_n^m - P_n^*). \tag{19}$$

By considering the relations of $m_1 P_1^* = m_2 P_2^* = \cdots = m_n P_n^*$, $m_1 P_1^m = m_2 P_2^m = \cdots = m_n P_n^m$ can be derived from (19). Therefore, it can be concluded that the active power can be shared in accordance with the ratio of droop coefficient (m_n), and these relations are not affected by hardware parameters. Moreover, as can be seen from (9), the steady-state value of the PCC voltage amplitude (E) is only related to m_n and P_n and has strong robustness against the line impedance and the virtual impedance. The adjustment of k_e can achieve a smaller steady-state voltage amplitude deviation. In addition, by taking the time derivative of (11) and considering the relation of $\dot{S}_{\mathrm{pn}}(t) = 0$, the error dynamic response

($\dot{e}_{\mathrm{pn}}(t) + c_1 e_{\mathrm{pn}}(t) = 0$) for the active power control loop can be obtained. By choosing the value of c_1 properly, the desired system dynamic can be easily designed by the first-order system ($\dot{e}_{\mathrm{pn}}(t) + c_1 e_{\mathrm{pn}}(t) = 0$).

The control efforts of the droop control module (U_n, δ_n) are synthesized into three-phase voltages at the voltage synthesis module and then are generated to the inner loop as its voltage commands (u_α^*,u_β^*), which can be seen from Figure 2. The capacitance voltage references ($u_{o\alpha}^*$,$u_{o\beta}^*$) can be derived by subtracting the voltage drops of the output currents ($i_{o\alpha}$, $i_{o\beta}$) on the virtual complex impedance ($Z_v = R_v + \mathrm{j}L_v$) from the voltage commands (u_α^*,u_β^*) [15]. In order to improve the dynamic performance and enhance the robustness of the inner loop, the next part focuses on the design of total-sliding-mode-based voltage controllers.

Remark 1. *Due to the simple structure, quadratic Lyapunov functions have been widely used for control-law design in various practical applications [22,23,32]. It is also adopted here as the design guidance of the control approach in this study. Note that, using a non-quadratic Lyapunov function usually leads to a better performance. Hosseinzadeh and Yazdanpanah [35] proposed a control scheme for robust adaptive tracking based on model reference adaptive control via a switching non-quadratic Lyapunov function with one degree of freedom (α). Similarly, a non-quadratic Lyapunov function was used for deriving a new adaptive law to improve the system tracking performance in [36]. Different values of α and their effect on the system response have been studied in [35,36], which revealed that using a multi-criterion α can improve the system tracking performance. Moreover, by using parameter projection modification, these new schemes are also robust against external disturbances. Thus, the control approaches based on non-quadratic Lyapunov functions have a great potential to improve the tracking performance and the system robustness, which is worthy to be investigated in the future work.*

3.2. TSMC-Based Voltage Control Scheme

As for the assumption of a balanced three-phase circuit, the dynamic equation in the two-phase static coordinate frame can be derived from Figure 2 and expressed as

$$\begin{cases} \ddot{u}_{o\alpha} = \frac{K_{\mathrm{PWM}}}{L_f C_f} u_{con\alpha} - \frac{r_f}{L_f}\dot{u}_{o\alpha} - \frac{1}{L_f C_f} u_{o\alpha} - \frac{1}{C_f}\dot{i}_{o\alpha} - \frac{r_f}{L_f C_f} i_{o\alpha} \\ \ddot{u}_{o\beta} = \frac{K_{\mathrm{PWM}}}{L_f C_f} u_{con\beta} - \frac{r_f}{L_f}\dot{u}_{o\beta} - \frac{1}{L_f C_f} u_{o\beta} - \frac{1}{C_f}\dot{i}_{o\beta} - \frac{r_f}{L_f C_f} i_{o\beta} \end{cases}, \tag{20}$$

where $u_{o\alpha}$ and $u_{o\beta}$ are the capacitance-voltage components of α and β axis, respectively; $u_{\mathrm{con}\alpha}$ and $u_{\mathrm{con}\beta}$ are the control signals; ($i_{o\alpha}$, $i_{o\beta}$) are output currents in α and β axis, respectively. The pulse-width-modulation (PWM) gain (K_{PWM}) is assumed to be 1 for the space-vector PWM (SVPWM). L_f, C_f and r_f are the filter inductor, the filter capacitor, and the equivalent series resistance (ESR) of the filter inductor, respectively. By choosing the capacitance voltages ($u_{o\alpha}$, $u_{o\beta}$) as the system states, and the control signals ($u_{\mathrm{con}\alpha}$, $u_{\mathrm{con}\beta}$) as the control inputs, (20) can be rearranged as (21). In (21), $\boldsymbol{x}(t) = [u_{o\alpha}\ u_{o\beta}]^T$; $\boldsymbol{u}(t) = [u_{\mathrm{con}\alpha}\ u_{\mathrm{con}\beta}]^T$; $\boldsymbol{z}(t) = [i_{o\alpha}\ i_{o\beta}]^T$; $a_{p1} = -r_f/L_f$; $a_{p2} = -1/(L_f C_f)$; $b_p = K_{\mathrm{PWM}}/(L_f C_f)$; $c_{p1} = -1/C_f$; $c_{p2} = -r_f/(L_f C_f)$; a_{p1n}, a_{p2n}, b_{pn}, c_{p1n}, and c_{p2n} denote the nominal values of a_{p1}, a_{p2}, b_p, c_{p1}, and c_{p2}, respectively; Δa_{p1n}, Δa_{p2n}, Δb_{pn}, Δc_{p1n} and Δc_{p2n} represent the system parameter uncertainties caused by the variations of the filter inductor (L_f), the filter capacitor (C_f), and the equivalent series resistance (ESR) (r_f). The vector of lumped-uncertainty components $\boldsymbol{d}_p(t)$ can be represented as (22), and Δa_{p1n}, Δa_{p2n}, Δb_{pn}, Δc_{p1n} and Δc_{p2n} can be expressed as (23)–(27), respectively.

$$\begin{aligned} \ddot{\boldsymbol{x}}(t) &= a_{p1}\dot{\boldsymbol{x}}(t) + a_{p2}x(t) + b_p\boldsymbol{u}(t) + c_{p1}\dot{\boldsymbol{z}}(t) + c_{p2}\boldsymbol{z}(t) = \left(a_{p1n} + \Delta a_{p1n}\right)\dot{\boldsymbol{x}}(t) \\ &+ \left(a_{p2n} + \Delta a_{p2n}\right)\boldsymbol{x}(t) + \left(b_{\mathrm{pn}} + \Delta b_{\mathrm{pn}}\right)\boldsymbol{u}(t) + \left(c_{p1n} + \Delta c_{p1n}\right)\dot{\boldsymbol{z}}(t) + \left(c_{p2n} + \Delta c_{p2n}\right)\boldsymbol{z}(t) \\ &= a_{p1n}\dot{\boldsymbol{x}}(t) + a_{p2n}\boldsymbol{x}(t) + b_{\mathrm{pn}}\boldsymbol{u}(t) + c_{p1n}\dot{\boldsymbol{z}}(t) + c_{p2n}\boldsymbol{z}(t) + \boldsymbol{d}_p(t), \end{aligned} \tag{21}$$

$$\boldsymbol{d}_p(t) = \Delta a_{p1n}\dot{\boldsymbol{x}}(t) + \Delta a_{p2n}\boldsymbol{x}(t) + \Delta b_{\mathrm{pn}}\boldsymbol{u}(t) + \Delta c_{p1n}\dot{\boldsymbol{z}}(t) + \Delta c_{p2n}\boldsymbol{z}(t). \tag{22}$$

$$\Delta a_{p1n} = -\frac{\Delta r_f L_{f0} - \Delta L_f r_{f0}}{L_{f0}\Big(L_{f0} + \Delta L_f\Big)}, \tag{23}$$

$$\Delta a_{p2n} = \frac{\Delta L_f C_{f0} + \Delta C_f L_{f0} + \Delta L_f \Delta C_f}{L_{f0} C_{f0}\Big(L_{f0} + \Delta L_f)(C_{f0} + \Delta C_f\Big)}, \tag{24}$$

$$\Delta b_{\mathrm{pn}} = -\frac{K_{PWM}\Big(\Delta L_f C_{f0} + \Delta C_f L_{f0} + \Delta L_f \Delta C_f\Big)}{L_{f0} C_{f0}\Big(L_{f0} + \Delta L_f)(C_{f0} + \Delta C_f\Big)}, \tag{25}$$

$$\Delta c_{p1n} = \frac{\Delta C_f}{C_{f0}\Big(C_{f0} + \Delta C_f\Big)}, \tag{26}$$

$$\Delta c_{p2n} = \frac{-\Delta r_f L_{f0} C_{f0} + \Delta C_f r_{f0} L_{f0} + \Delta L_f r_{f0} C_{f0} + \Delta L_f \Delta C_f r_{f0}}{L_{f0} C_{f0}\Big(L_{f0} + \Delta L_f)(C_{f0} + \Delta C_f\Big)}, \tag{27}$$

where (L_{f0}, C_{f0}, r_{f0}) denote the nominal values of (L_f, C_f, r_f), respectively; (ΔL_f, ΔC_f, Δr_f) represent the variations of (L_f, C_f, r_f), respectively.

As for a real circuit, the deviations of the filter inductor (L_f) and the filter capacitor (C_f) are limited to ±20%, and the equivalent series resistance (r_f) of the filter inductor is small enough to be neglected. Moreover, the output control efforts are always limited by hardware digital/analog (D/A) ports, even for the divergence of the designed control input ($\boldsymbol{u}_{\mathrm{con}}$) in (30). For practical applications, the time derivative term ($\Delta a_{p1n}\dot{x}(t)$) is derived in a discrete form ($\Delta a_{p1n}(\boldsymbol{x}(k) - \boldsymbol{x}(k-1))/T_{\mathrm{s}}$), where k is the sampling instant and T_s is the sampling period. The sampling period T_s is not infinitesimal, which has a value of 0.0001 s, corresponding to a sampling frequency of 10 kHz. Therefore, the time derivative term ($\Delta a_{p1n}\dot{x}(t)$) is bounded. Similarly, the time derivative term ($\Delta c_{p1n}\dot{z}(t)$) is also bounded. Thus, the disturbance term in (22) can be reasonably assumed to be bounded by a positive constant for a real system. Here, the bound of $\boldsymbol{d}_p(t)$ is assumed to be given, i.e.,

$$\left\|\boldsymbol{d}_p(t)\right\|_1 \leq \rho, \tag{28}$$

where $\|\cdot\|_1$ represents the one-norm operator and ρ is given a positive constant.

The objective of the voltage closed-loop control is to achieve a zero steady-state tracking error between the system state $\boldsymbol{x}(t)$ and the reference voltage $\boldsymbol{x}_d$, where $\boldsymbol{x}_d = [u^*_{o\alpha}\ u^*_{o\beta}]^T$. By considering the superiority on the nonlinear robust control and the insensitivity of the parameter variations and external disturbances, a TSMC framework is developed in this study for the capacitance voltage control. Define a proportion-integration-differentiation (PID)-type sliding surface as

$$\boldsymbol{S}(t) = \dot{\boldsymbol{e}}_v(t) + k_1\boldsymbol{e}_v(t) + k_2\int_0^t \boldsymbol{e}_v(\tau)d\tau - \dot{\boldsymbol{e}}_v(0) - k_1\boldsymbol{e}_v(0), \tag{29}$$

where the tracking error vector is denoted as $\boldsymbol{e}_v(t) = \boldsymbol{x}_d - \boldsymbol{x}$; $\dot{e}_v(0)$ and $\boldsymbol{e}_v(0)$ are initial values of $\dot{e}_v(t)$ and $\boldsymbol{e}_v(t)$, respectively; k_1 and k_2 are given positive constants. Following the design principle of a TSMC controller, the TSMC-based voltage control law $\boldsymbol{u}_{\mathrm{con}} = [u_{\mathrm{con}\alpha}\ u_{\mathrm{con}\beta}]^T$ can be designed as

$$\boldsymbol{u}_{\mathrm{con}} = \boldsymbol{u}_b + \boldsymbol{u}_c, \tag{30}$$

where $\boldsymbol{u}_b = [u_{b\alpha}\ u_{b\beta}]^T$ is the vector of baseline model control laws, which is designed as (31); $\boldsymbol{u}_c = [u_{c\alpha}\ u_{c\beta}]^T$ is the vector of additional curbing control laws, which is designed as (32).

The object of the curbing control design is to totally eliminate the unpredictable perturbation effect from the parameter variations and external disturbances so that the baseline model design performance can be exactly assured.

$$\boldsymbol{u}_b = b_{\mathrm{pn}}^{-1}\left(\ddot{\boldsymbol{x}}_d - a_{p1n}\dot{\boldsymbol{x}} - a_{p2n}\boldsymbol{x} - c_{p1n}\dot{\boldsymbol{z}} - c_{p2n}\boldsymbol{z} + k_1\dot{\boldsymbol{e}}_v + k_2\boldsymbol{e}_v\right), \tag{31}$$

$$\boldsymbol{u}_c = \rho b_{\mathrm{pn}}^{-1}\mathrm{sgn}(\boldsymbol{S}(t)) + k_3 b_{\mathrm{pn}}^{-1}\boldsymbol{S}(t), \tag{32}$$

where k_3 is helpful to reduce the chattering phenomena in the control signal vector $\boldsymbol{u}_{\mathrm{con}}$ and is given a positive constant.

By combining (21), (29) and (30), one can obtain $\boldsymbol{S}^T(t)\dot{\boldsymbol{S}}(t) < 0$. Therefore, the asymptotic stability of the TSMC system can be guaranteed without the impact of system uncertainties, and the sliding motion can be assured during the whole control period. The flowchart for the design process of the proposed TSMC-based control structure is depicted in Figure 3. The effectiveness of the proposed TSMC scheme can be verified by the numerical simulations and experimental results in Section 5.

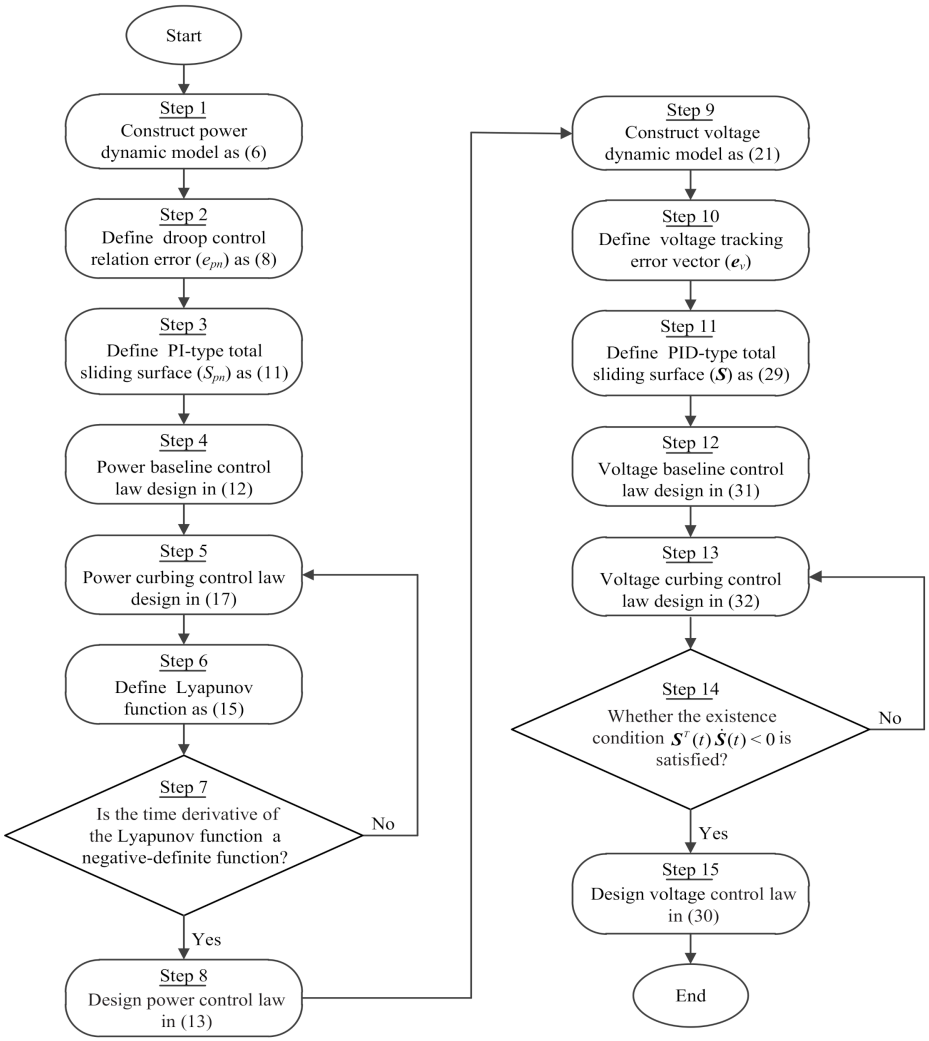

Figure 3. Design flowchart of proposed total sliding-mode control (TSMC)-based control structure.

4. Small-Signal Model and Stability Analysis

To analyze the influence of control parameters on the system stability, a small-signal model of the TSMC-based droop control method is established. Based on the power flow

characteristics and the low-pass filter, the expression of the active and reactive power can be derived as

$$\begin{cases} \dot{P}_n^m = -\omega_f P_n^m + \omega_f k_{\text{pun}}(U_n - E) \\ \dot{Q}_n^m = -\omega_f Q_n^m + \omega_f k_{q\delta}(\delta_n - \delta_c) \end{cases}. \tag{33}$$

Therefore, the small-signal model of the active and reactive power can be expressed as

$$\begin{cases} \Delta\,\dot{P}_n^m = -\omega_f \Delta P_n^m + \omega_f k_{\text{pun}}(\Delta U_n - \Delta E) \\ \Delta\,\dot{Q}_n^m = -\omega_f \Delta Q_n^m + \omega_f k_{q\delta}(\Delta \delta_n - \Delta \delta_c) \end{cases}. \tag{34}$$

Based on the control efforts in (13), the small-signal model of the TSMC-based droop controller can be given as

$$\begin{cases} \Delta\,\dot{U}_n = (a_1 + a_4 b_1)\Delta P_n^m + (a_2 + a_4 b_2) + (a_3 + a_4 b_3)\Delta E \\ \Delta\,\delta_{.n} = n_n \Delta Q_n^m \end{cases}, \tag{35}$$

where $a_1 = \left[-\omega_f^2 + \omega_f(c_1 + c_2) - c_1 c_2\right]/(\omega_f k_{\text{pu}})$, $a_2 = \omega_f - c_1 - c_2$, $b_2 = -m_n \omega_f k_{\text{pu}}/k_e$, $a_3 = -\left[\omega_f + c_1 c_2 k_e/(m_n \omega_f k_{\text{pu}}\right) - c_1 - c_2]$, $a_4 = \left[m_n \omega_f k_{\text{pu}} - k_e(c_1 c_2)\right]/(m_n \omega_f k_{\text{pu}})$, $b_1 = \left[m_n \omega_f (c_1 + c_2) - m_n c_1 c_2\right]/[k_e(c_1 + c_2)]$, $b_3 = -\left[k_e c_1 c_2 - m_n \omega_f k_{\text{pu}}(c_1 + c_2)\right]/[k_e(c_1 + c_2)]$. The power control model contains four state variables, and the small-signal model of the system can be represented as

$$\left[\Delta \dot{\boldsymbol{X}}\right] = \boldsymbol{A}[\Delta \boldsymbol{X}] + \boldsymbol{B}\left[\ \Delta E \quad \Delta \delta_c\ \right]^T, \tag{36}$$

where $[\Delta \boldsymbol{X}]=[\Delta P_n^m\ \Delta Q_n^m\ \Delta U_n\ \Delta \delta_n]^T$, and

$$\boldsymbol{A} = \begin{bmatrix} -\omega_f & 0 & \omega_f k_{\text{pu}} & 0 \\ 0 & -\omega_f & 0 & \omega_f k_{q\delta} \\ a_1 + a_4 b_1 & 0 & a_2 + a_4 b_2 & 0 \\ 0 & n_n & 0 & 0 \end{bmatrix}, \tag{37}$$

$$\boldsymbol{B} = \begin{bmatrix} -\omega_f k_{\text{pu}} & 0 & a_3 + a_4 b_3 & 0 \\ 0 & -\omega_f k_{q\delta} & 0 & 0 \end{bmatrix}^T. \tag{38}$$

Based on the small-signal model of the TSMC-based droop control method, the influence of control parameters on the system stability and dynamic performance can be observed from the root locus of $\boldsymbol{A}$. By the method of control variates, for each case, one parameter is varied in a preset range, and other relevant parameters remain unchanged, which are set as the same as the ones in Table 2. Figures 4–6 show the system dominant root locus with respect to the variations of droop parameters (m and n), TSMC controller parameters (c_1 and c_2) and the feedback parameter (k_e), respectively. The value of m is varied in the range of $[1 \times 10^{-6}, 1]$ in Figure 4a; the value of n is varied in the range of $[1 \times 10^{-6}, 1 \times 10^{-1}]$ in Figure 4b; the value of c_1 is varied in the range of [1, 10,000] in Figure 5a; the value of c_2 is varied in the range of [1, 10,000] in Figure 5b; the value of k_e is varied in the range of [1, 50] in Figure 6. As can be seen from Figure 4a, when the value of m is relatively small, the system presents a nearly second-order underdamped behavior with a pair of conjugate complex dominant roots and a too small value of m will lead to a poor stability margin. As the value of m gradually increases, the dominant eigenvalues move away from the imaginary axis, and the system stability is enhanced. However, a too big value of m may lead to the system oscillation. By considering the voltage drop, the value of m is limited. As can be seen from Figure 4b, when a small n is adopted, the dominant eigenvalues are located on the negative real axis, and the system is overdamped with a poor dynamic response. As the value of n increases, the dominant root moves

away from the imaginary axis, and the system dynamic is improved. When the value of n increases to a certain value, the system presents a nearly second-order underdamped behavior. However, a too big value of n will lead to the system oscillation.

Table 2. Detail system parameters.

Parameter	Value
DC Voltage	U_{dc} =700 V
AC Phase Voltage	220 V(RMS)/60 Hz
Sampling Frequency	10 kHz
LC Filter	L_f = 1.4 mH, C_f = 20 μF, r_f = 0.0471 Ω
Line Impedance	R_{line1} = 2 Ω, L_{line1} = 2.5 mH, R_{line2} = 1 Ω, L_{line2} = 1.4 mH
Voltage Controller (TSMC)	k_1 = 13,000, $k_2 = 8.5 \times 10^7$, ρ = 60, k_3 = 2000 $\dot{e}_{v\alpha}(0) = 0$, $e_{v\alpha}(0) = 13462$,$\dot{e}_{v\beta}(0) = 0$, $e_{v\beta}(0) = 0$
Basic Droop Control Gains	$m_1 = m_2 = 6 \times 10^{-3}$, $n_1 = n_2 = 2 \times 10^{-3}$
TSMC-based Droop Controller	c_1 = 300, K = 100, c_2 = 500, $e_{pn}(0)$ = 3140, k_e = 10
Virtual Complex Impedance	$R_{v1} = R_{v2}$ = 0.2 Ω, L_{v1} = −2.5 mH, L_{v2} = −1.4 mH
Power Rating	P^* = 5 kW, Q^* = 5 kVar

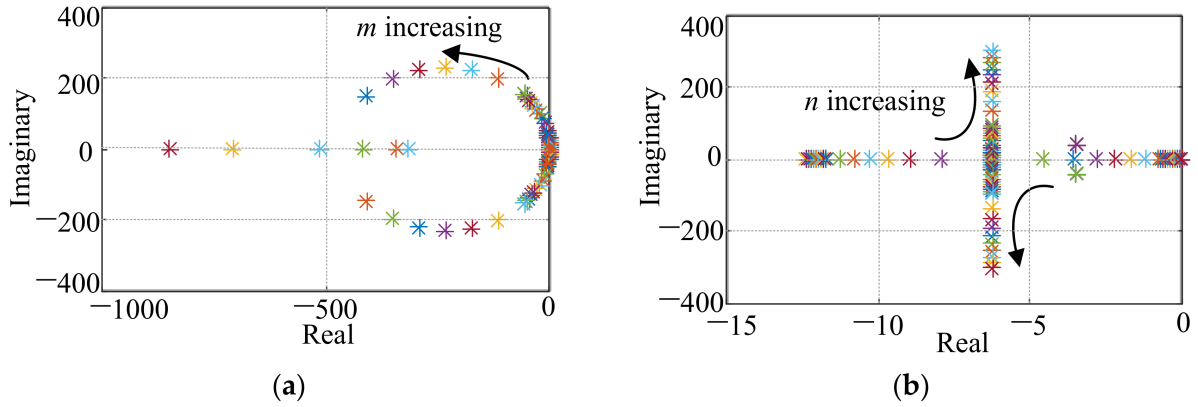

Figure 4. System dominant root locus at (**a**) $m \in [1 \times 10^{-6}, 1]$; (**b**) $n \in [1 \times 10^{-6}, 1 \times 10^{-1}]$.

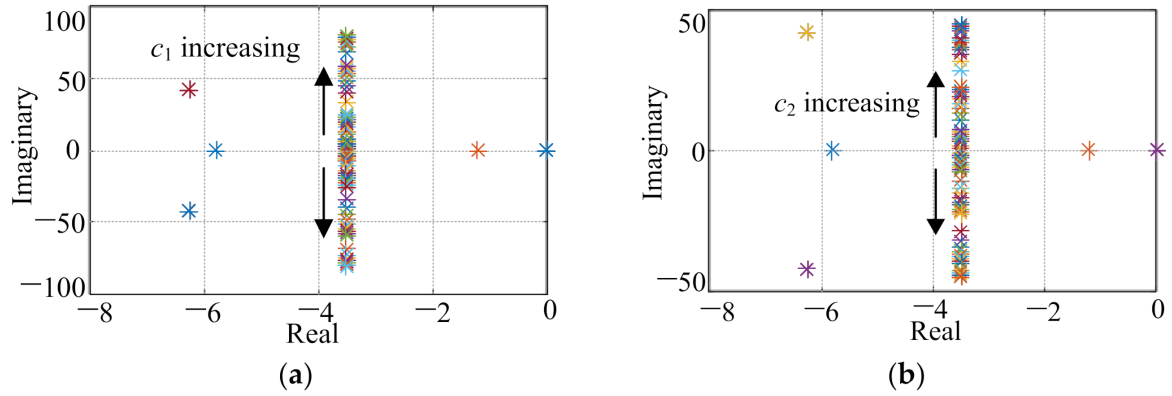

Figure 5. System dominant root locus at (**a**) $c_1 \in [1, 10{,}000]$; (**b**) $c_2 \in [1, 10{,}000]$.

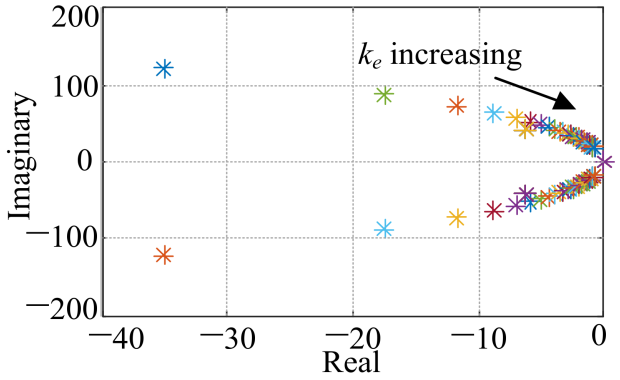

Figure 6. System dominant root locus at $k_e \in [1, 50]$.

Figure 5 shows the system dominant root locus when the TSMC controller parameters (c_1 and c_2) vary in the range of [1, 10,000]. As can be seen from Figure 5, the system presents a second-order underdamped behavior with a pair of conjugate complex roots. As the value of c_1 increases, the system damping is reduced. The influence of the parameter (c_2) on the dominant root locus is similar as that of c_1. By considering the tracking performance, the values for c_1 and c_2 can be properly selected. Note that, for the TSMC based droop control method, the influence of droop parameters (m and n) on the system stability and the dynamic performance may be slightly different from the traditional droop control method. By following the aforementioned analyses, the droop parameters (m and n) can be designed.

The dominant root locus of the TSMC-based droop-controlled system with respect to the variations of k_e is depicted in Figure 6. As can be seen from Figure 6, the system presents a nearly second-order underdamped behavior with a pair of conjugate complex dominant roots. As the value of k_e increases during the range of [1, 50], the dominant eigenvalues move towards the imaginary axis, and the stability margin is reduced. Therefore, the value of $k_e = 10$ is selected in this study by comprehensively considering the system stability and voltage quality.

5. Numerical Simulations and Experimental Results

In order to verify the effectiveness of the proposed total-sliding-mode-control (TSMC)-based voltage stabilization and power sharing scheme for the parallel-connected inverters of islanded micro-grid (MG), numerical simulations and experimental studies are conducted in this section. Firstly, some simulation results are provided to verify the power sharing performance of the proposed method and the influences of the control parameters analyzed in Section 4. Then, some comparative experimental results of the proposed TSMC-based *P-U/Q-f* droop controller with a conventional *P-U/Q-f* droop controller in [11] and a proportional-integral (PI)-based *P-U/Q-f* droop controller in [15] are provided to exhibit the superior of the proposed method.

5.1. Numerical Simulations

According to the system model of parallel-connected inverters in Figure 1 and the detailed system parameters in Table 2, numerical simulations are carried out via the MATLAB software (Version 2016b, MathWorks, Natick, MA, USA).

As for a real circuit, the deviations of the filter inductor (L_f) and the filter capacitor (C_f) are limited to ±20%, and the equivalent series resistance (r_f) of the filter inductor is small enough to be neglected. By considering the value of the filter inductor (L_f) and the filter capacitor (C_f) deviating 20% and using the parameters in Table 2, the estimated value of $\|\boldsymbol{d}_p(t)\|_1 > \rho$ can be calculated according to (22). The theoretical bound value of $\|\boldsymbol{d}_p(t)\|_1 > \rho$ can be roughly obtained to be about 1.4×10^{10}. Therefore, a big value of ρ is required to bound the disturbance term defined in (22), which may cause the chattering

phenomena in the control effort (32). Fortunately, the term of $k_3 \boldsymbol{S}(t)/b_{pn}$ added in the curbing control law (32) is helpful to reduce the chattering phenomena introduced by the sign function. It is because the increasing of k_3 properly can dominate the fact that $\boldsymbol{S}^T(t)\dot{\boldsymbol{S}}(t) = -k_3 \boldsymbol{S}^T(t)\boldsymbol{S}(t) < 0$, even the worst case $\|\boldsymbol{d}_p(t)\|_1 > \rho$ happens. Therefore, the parameter ρ could be conservatively selected to avoid the increasing of the chattering phenomena caused by the sign-function term $\rho \mathrm{sgn}(\boldsymbol{S}(t))/b_{pn}$ in (32).

By considering the value of the line resistance deviating 50% and the voltage amplitude difference between DG_n and the point of common coupling to be 15 V, the estimated value of $|D_{pn}|$ can be calculated according to (7). By using the parameters in Table 2, one can roughly obtain the theoretical bound value of $|D_{pn}|$ to be about 5.8×10^4. However, the selection of a large value of K will cause serious chattering phenomena in the control effort. Fortunately, the chattering phenomena caused by the sign function can be alleviated by an additional sliding-surface term $(c_2 S_{pn}(t)/(m_n \omega_f k_{pun}))$ in the curbing control law (17). As can be seen in (18), the term $-c_2 S_{\mathrm{pn}}^2(t)$ can dominate the fact of $\dot{V}_P < 0$ even the worst cased $|D_{pn}| > K$ happens, which means that the parameter K could be conservatively selected to avoid increasing the chattering phenomena caused by the sign-function term of $K\mathrm{sgn}(S_{pn}(t))/(m_n \omega_f k_{pun})$.

5.1.1. Power Sharing Performance Verification

Since the frequency is a global variable, the reactive power sharing can be achieved by the resistive *P-U/Q-f* droop control method. This study mainly focuses on improving the active power sharing performance for a resistive *P-U/Q-f* droop-controlled system. Figure 7 shows the simulation results of output active power and voltage amplitude with the proposed TSMC-based *P-U/Q-f* droop controller. In this figure, the inverter 1 starts with a load of 2 kW active power, and then, the inverter 2 is connected to the system to share the power at 0.4 s. In order to examine the system regulation capability under load changes, a load of 2 kW active power is suddenly injected to the system of parallel-connected inverters at 0.8 s, and removed at 1.2 s. As can be seen from Figure 7a, although the line impedances of the parallel-connected inverters differ a lot from each other, the TSMC-based *P-U/Q-f* droop control method still can ensure an accurate active power sharing in both the transient and steady states and shows less sensibility to the line impedance difference and load variations. Moreover, Figure 7b shows that the deviation rates of the voltage amplitude before and after load variation can be reduced to 0.77% and 0.58% by the proposed TSMC-based *P-U/Q-f* droop control method, and the corresponding voltage amplitude variation is only 0.6 V. It is obvious that the proposed TSMC-based *P-U/Q-f* droop control method has a good performance of power sharing and voltage stabilization. Then, the influences of the control parameters on power sharing performance are verified.

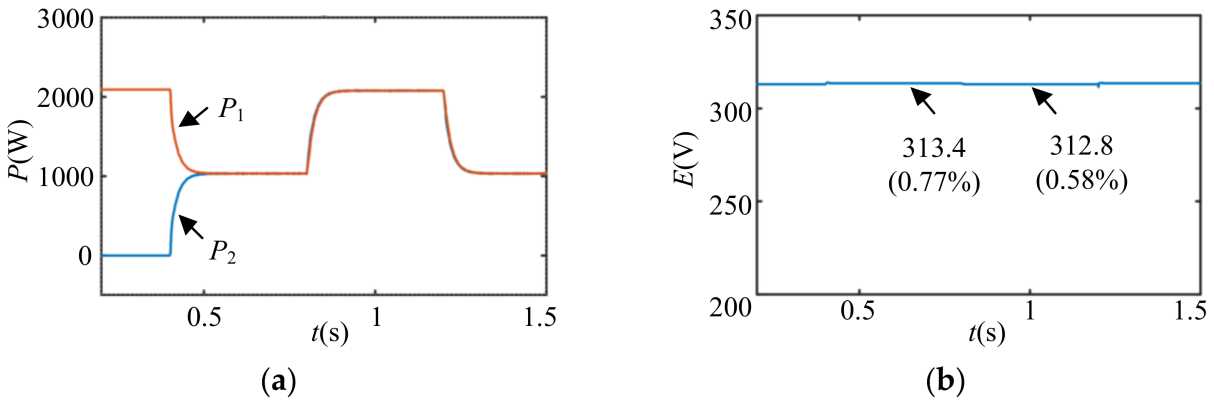

Figure 7. Numerical simulation results with proposed TSMC-based *P-U/Q-f* droop controller: (**a**) active power sharing of parallel-connected inverters; (**b**) voltage amplitude of point of common coupling (PCC) voltage.

5.1.2. Influence of k_e, m and n on Power Sharing Performance

The power sharing performances at a smaller and a bigger parameter values (k_e, m and n) are descripted in Figure 8, where other relevant parameters are the same as the ones in Table 2. In Figure 8a,b, the values of k_e are set as 1 and 25, respectively. In Figure 8c,d, the values of m are set as $m = 6 \times 10^{-4}$ and $m = 6 \times 10^{-2}$, respectively. In Figure 8e,f, the values of n are set as $n = 2 \times 10^{-4}$ and $n = 5 \times 10^{-2}$, respectively. Moreover, two inverters share a load of 2 kW active power before 2 s; another load of 2 kW active power and 1 kVar reactive power are suddenly injected at 2 s and removed at 2.5 s. As can be seen from Figure 8a,b, the system is stable with a good power sharing performance when a smaller value of k_e is adopted. When the value of k_e is increased to $k_e = 25$, the system stability cannot be ensured. As can be seen from Figure 8c, a too small value of m will result in an unstable system. The reasons are the dominant eigenvalues to be near the imaginary axis, and the damping effect to be poor. As the value of m increases, the damping effect can be enhanced, and the system can remain stable even with a big value of m, which can be seen from Figure 8d. When a small value of n is adopted, as can be seen from Figure 8e, the dynamic response of the reactive power is deteriorated because the system presents an overdamped behavior with the dominant eigenvalues located on the negative real axis. A big value of n will lead to an unstable system, as can be seen in Figure 8f.

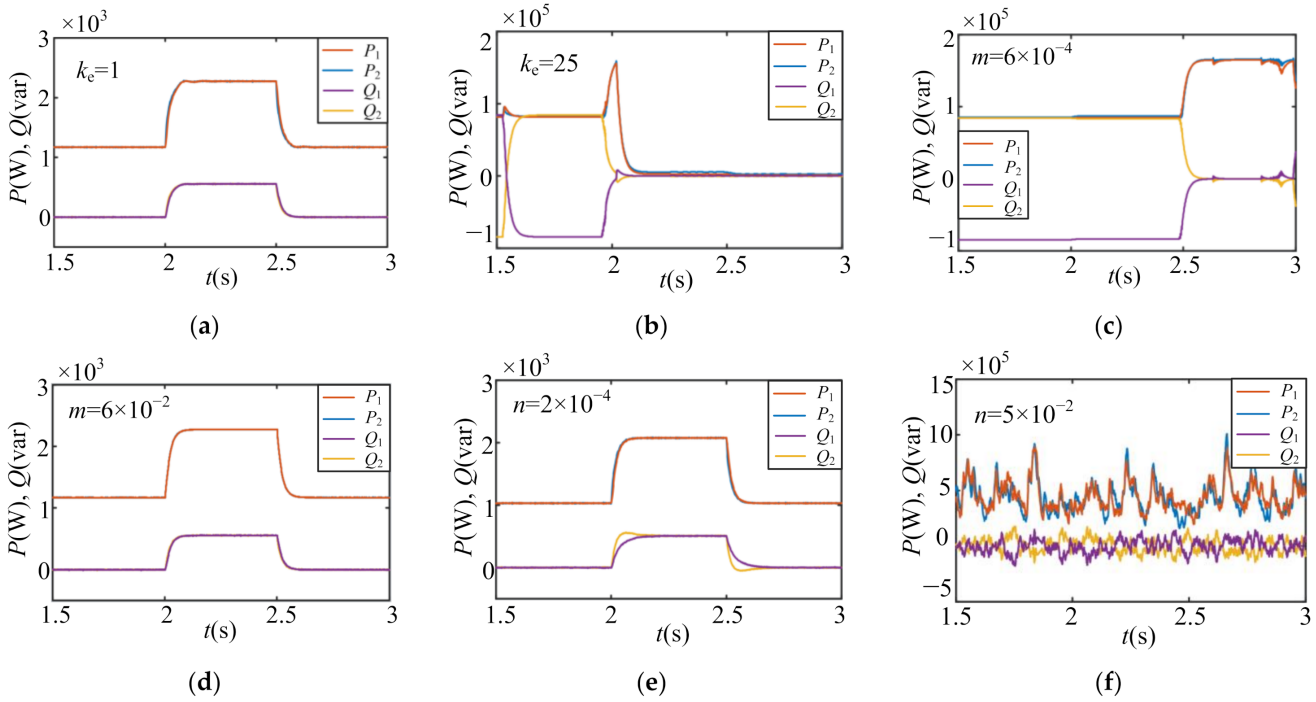

Figure 8. Power response at different parameter values (k_e, m and n) of proposed TSMC-based *P-U/Q-f* droop controller: (**a**) $k_e = 1$; (**b**) $k_e = 25$; (**c**) $m = 6 \times 10^{-4}$ and $n = 2 \times 10^{-3}$; (**d**) $m = 6 \times 10^{-2}$ and $n = 2 \times 10^{-3}$; (**e**) $m = 6 \times 10^{-3}$ and $n = 2 \times 10^{-4}$; (**f**) $m = 6 \times 10^{-3}$ and $n = 5 \times 10^{-2}$.

5.1.3. Influence of c_1 and c_2 on Power Sharing Performance

Figure 9 shows numerical simulations of active and reactive power sharing performance with the proposed TSMC-based *P-U/Q-f* droop controller when a smaller and a bigger parameter values (c_1 and c_2) are selected, and other relevant parameters are the same as the ones in Table 2. In Figure 9a,b, the value of $c_2 = 500$ is fixed, and the values of c_1 are set as $c_1 = 60$ and $c_1 = 600$, respectively. Similarly, the value of $c_1 = 300$ is fixed, and the value of c_2 are set as $c_2 = 200$ and $c_2 = 1300$ in Figure 9c,d, respectively. Moreover, two inverters share a load of 2 kW active power before 2 s; another load of 2 kW active power and 1 kVar reactive power are suddenly injected at 2 s, and removed at 2.5 s. When a smaller value of

c_1 is adopted, as can be seen from Figure 9a, the dynamic performance of the active power sharing is deteriorated and a too small value of c_1 will lead to a poor tracking performance. As the value of c_1 increases, the dynamic performance can be improved. However, the system will be unstable when a too big value of c_1 is selected, which can be seen from Figure 9b. On the other hand, the influence of c_2 is similar as that of c_1, which can be seen from Figure 9c,d.

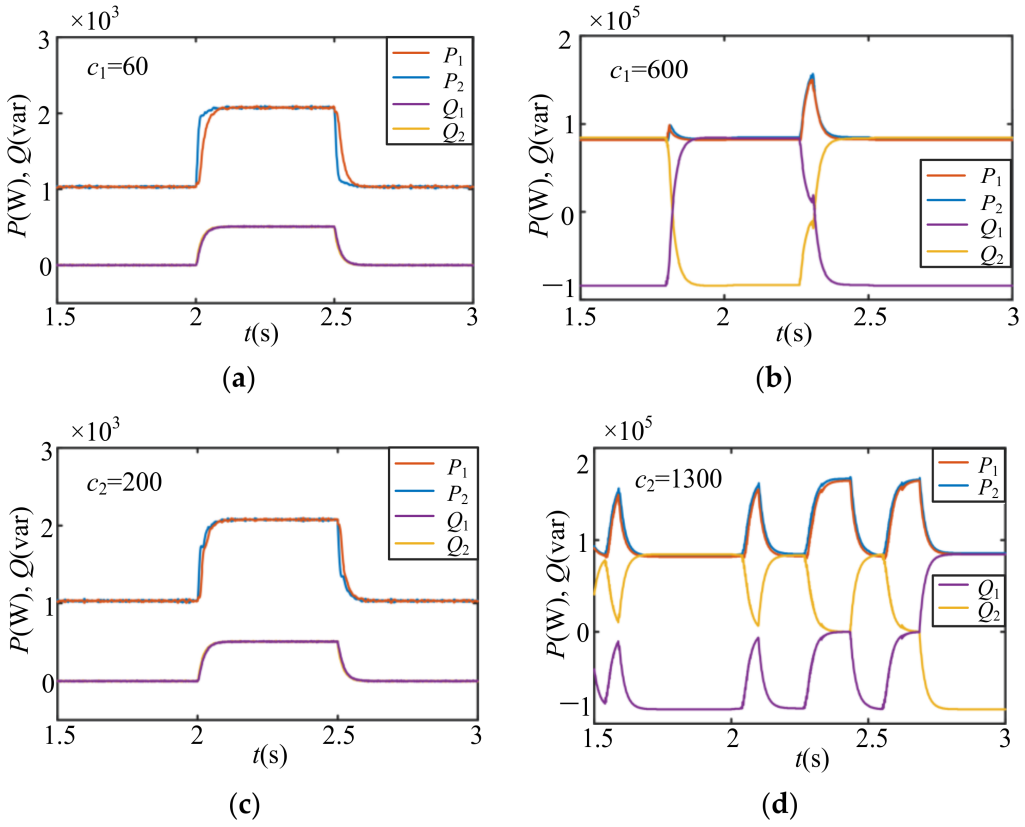

Figure 9. Power response at different parameter values (c_1 and c_2) of proposed TSMC-based *P-U*/*Q-f* droop controller: (**a**) c_1 = 60 and c_2 = 500; (**b**) c_1 = 600 and c_2 = 500; (**c**) c_1 = 300 and c_2=200; (**d**) c_1 = 300 and c_2 = 1300.

The corresponding power allocation errors can be calculated by (39) [14], and the power sharing performance can be represented by the records of the root-mean-squared error (RMSE).

$$\begin{cases} e_{\text{ap}} = (m_1P_1 - m_2P_2)/m_2P_2^* \times 100\% \\ e_{\text{aq}} = (n_1Q_1 - n_2Q_2)/n_2Q_2^* \times 100\% \end{cases} \tag{39}$$

Figure 10 shows the RMSE values of power allocation errors with different values of c_1 and c_2. As can be seen from Figure 10, the active power sharing error can be reduced by increasing the value of c_1 or c_2. However, the system will be unstable when a too big value of c_1 or c_2 is selected.

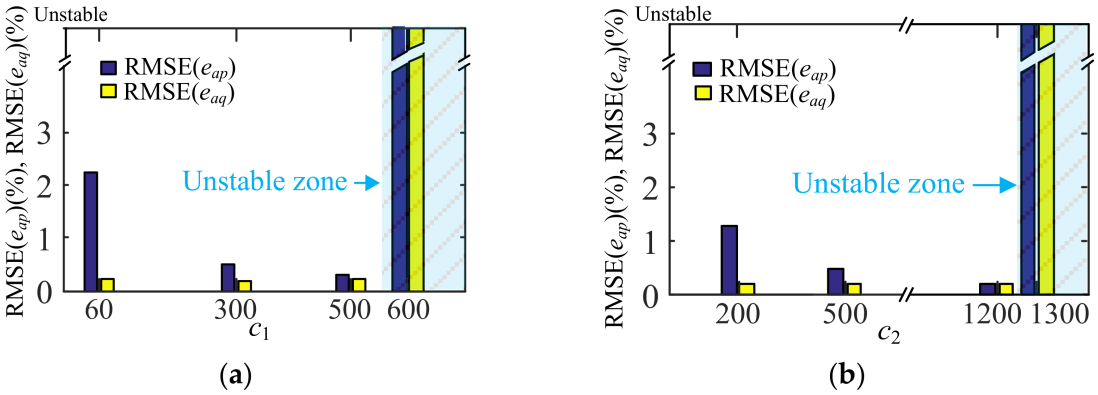

Figure 10. Numerical simulation results of power allocation errors at different parameter values (c_1 and c_2) of proposed TSMC-based *P-U/Q-f* droop controller: (**a**) c_1 varying; (**b**) c_2 varying.

5.1.4. Influence of K and c_2 on Chattering Phenomena

In order to examine the influence of the values of K and c_2 on the control chattering phenomena, numerical simulations of the parallel-connected inverter system operated from Case 1 to Case 3 are depicted in Figure 11. In Figure 11, the value of c_1 is fixed at $c_1 = 300$; the values of K and c_2 are respectively selected as $K = 5000$ and $c_2 = 0$ for Case 1; $K = 20{,}000$ and $c_2 = 0$ for Case 2; $K = 100$ and $c_2 = 500$ for Case 3, and other relevant parameters are the same as the ones in Table 2. As can be seen from Figure 11 at Case 1, with $K = 5000$ and $c_2 = 0$, no chattering phenomena can be observed in the waveforms of the control effort in Figure 11b. However, a relatively big tracking error exists in Figure 11a, which will lead to a poor performance in the active power sharing and the PCC voltage restoration, which can be seen from Figure 11c,d. To a certain extent, one can reduce the tracking error by increasing K. However, the ability of K on suppressing the tracking error is limited, and the chattering phenomena appears as K continues to increase, which can be seen from Figure 11a at Case 2. By adding the parameter of c_2 and decreasing the value of K, Case 3 shows the waveforms with $K = 100$ and $c_2 = 500$. A good tracking performance with a small tracking error and without chattering phenomena can be achieved. Thus, the existence of c_2 can alleviate the contradiction of the tracking error and the chattering phenomena. By this way, an accurate power sharing precision and good voltage restoration property can be obtained. The influence of the values of ρ and k_3 on the control chattering phenomena is similar as that of K and c_2, which can refer to Figure 11.

5.1.5. Comparison Study

The performance of the proposed TSMC-based droop control method in this study is compared with the improved washout-filter-based method in [18] under the same conditions as in Section 5.1.1, and the corresponding results are summarized in Table 3. For both methods, the rated active power in the droop controller is set to be 0 kW. As can be seen from Table 3, the proposed method in this study can achieve a smaller PCC voltage deviation, and the voltage deviation rate can be reduced by more than 67.5% in comparison with the improved washout-filter-based method in [18]. Moreover, when the line impedances of parallel inverters differ from each other, a good power sharing performance with strong robustness against line impedance still can be achieved by the proposed method in this study. However, the power sharing performance will be deteriorated when the improved washout-filter-based method in [18] is adopted. In addition, the proposed TSMC-based droop control method can provide the system with a shorter convergent time of about 0.04 s in comparison with 0.1s for the improved washout-filter-based method in [18].

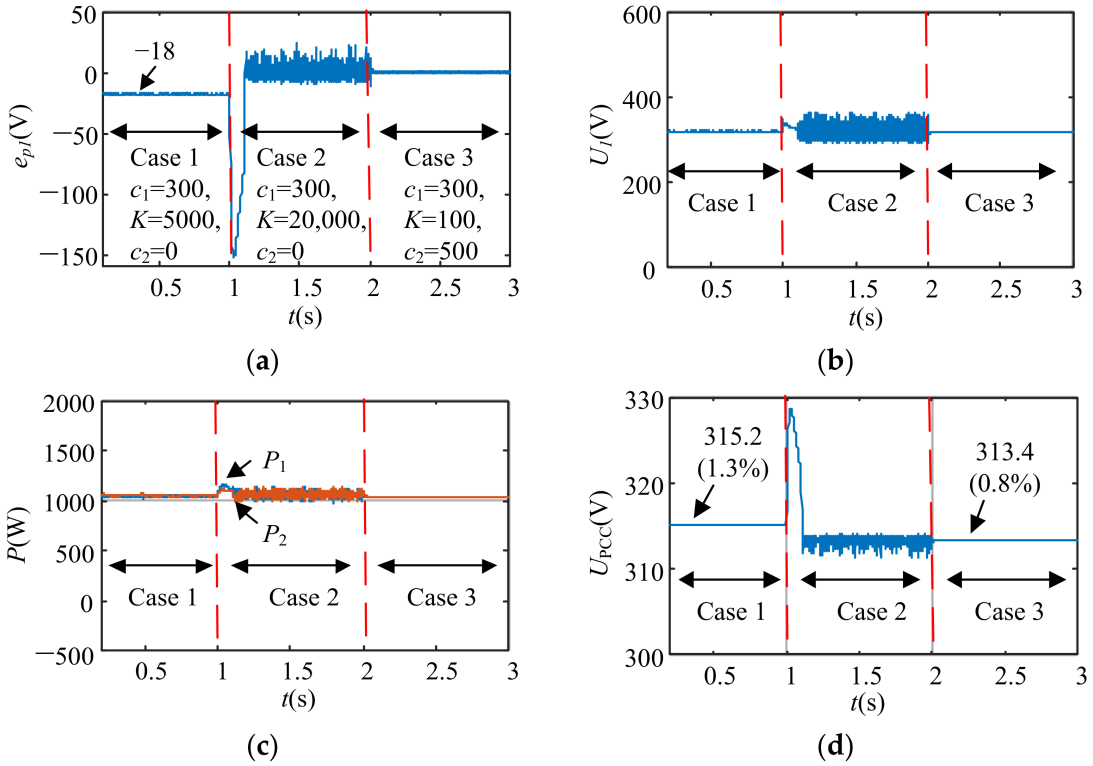

Figure 11. Waveforms with proposed TSMC-based power and voltage controller at different values of K and c_2: (**a**) droop control relation error (e_{p1}); (**b**) control effort of power control loop (U_1); (**c**) active power sharing of parallel inverters; (**d**) voltage amplitudes of PCC voltage.

Table 3. Performance comparisons of proposed method in this study and improved washout-filter-based method in [18].

Operational Objectives	Test Conditions	Improved Washout-Filter-Based Method in [18]	Proposed TSMC-Based Droop Control Method
Voltage quality	PCC voltage deviation rate PCC voltage variation rate	−0.77%/−1.2% −0.45%	−0.19%/−0.39% −0.19%
Power sharing performance	With same line impedance With different line impedance	Good Deteriorated	Good Good
Settling time	——	0.1 s	0.04 s

5.2. Experimental Results

A prototype of parallel-connected inverters in Figure 12 has been constructed to verify the effectiveness of the proposed method. Two voltage-source inverters (VSIs) are separately controlled by two digital microcontrollers, which consist of a main algorithm controller via a DSP (TMS320F28335) and an auxiliary controller via an FPGA (XC3S400). The experimental control parameters are the same as the ones in Table 2. In the experimental tests, a three-phase resistor load of 50 Ω is used, and an extra three-phase resistor load of 30 Ω is employed for load variations.

5.2.1. Performance Verification of TSMC-Based Voltage Controller

First, the voltage tracking performance of the system with the quasi-proportional-resonant controller (quasi-PRC) and the proposed total sliding-mode controller (TSMC) are compared and depicted in Figure 13. As can be seen from Figure 13, the system with the TSMC shows good dynamic performance with a convergent time of 3ms, which is shorter than 12ms for the quasi-PRC. Since the voltage tracking performance can be reflected by the records of the root-mean-squared error (RMSE), the voltage RMSEs with the two methods are calculated as RMSE ($e_{v\alpha}$) = 6.090 and RMSE ($e_{v\beta}$) = 5.957 for the quasi-PRC scheme;

RMSE ($e_{v\alpha}$) = 2.468 and RMSE ($e_{v\beta}$) = 4.105 for the proposed TSMC framework. It is obvious that a better voltage tracking property can be obtained by the proposed TSMC.

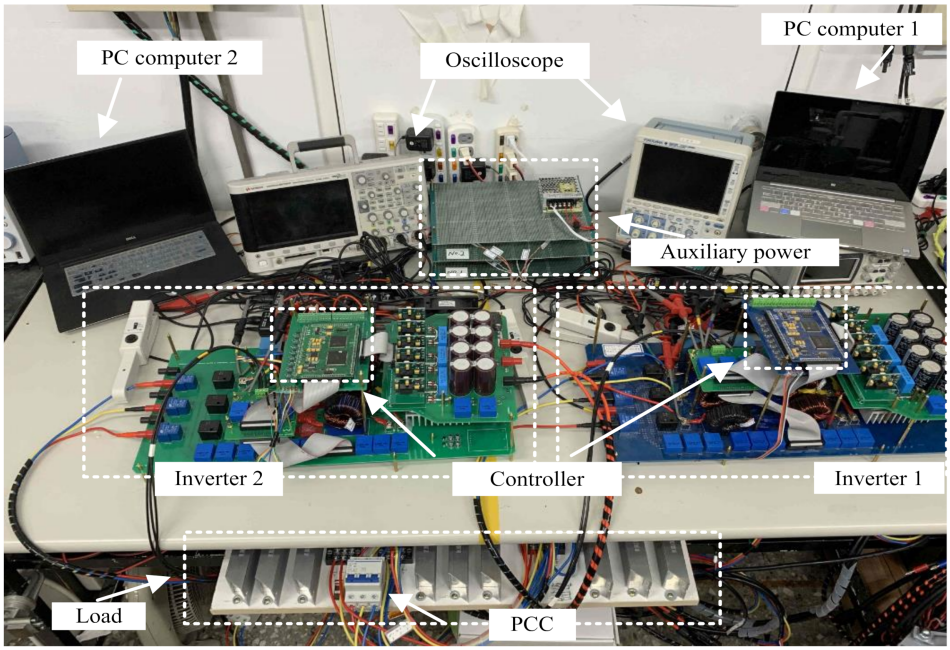

Figure 12. Experimental prototype.

Figure 14 shows the experimental results of the inverter output voltage and current responses with the quasi-PRC and the TSMC under load variations. As can be seen from Figure 14, the reliability of the proposed TSMC framework can be guaranteed under load variations, and smaller values of RMSE($e_{v\alpha}$) = 1.166 and RMSE($e_{v\beta}$) = 1.552 can be obtained in comparison with RMSE($e_{v\alpha}$) = 1.589 and RMSE($e_{v\beta}$) = 1.998 for the quasi-PRC.

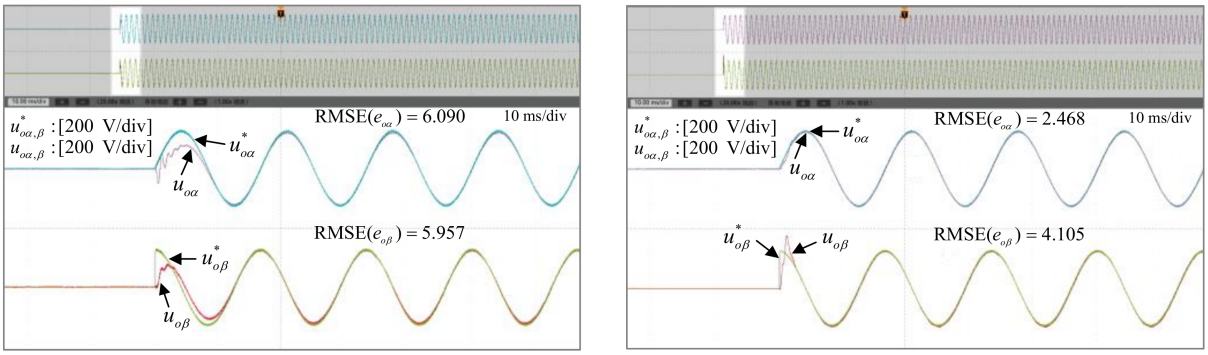

Figure 13. Experimental waveforms of voltage commands ($u^*_{o\alpha}$, $u^*_{o\beta}$) and output voltages ($u_{o\alpha}$, $u_{o\beta}$): (**a**) quasi-PRC; (**b**) proposed TSMC.

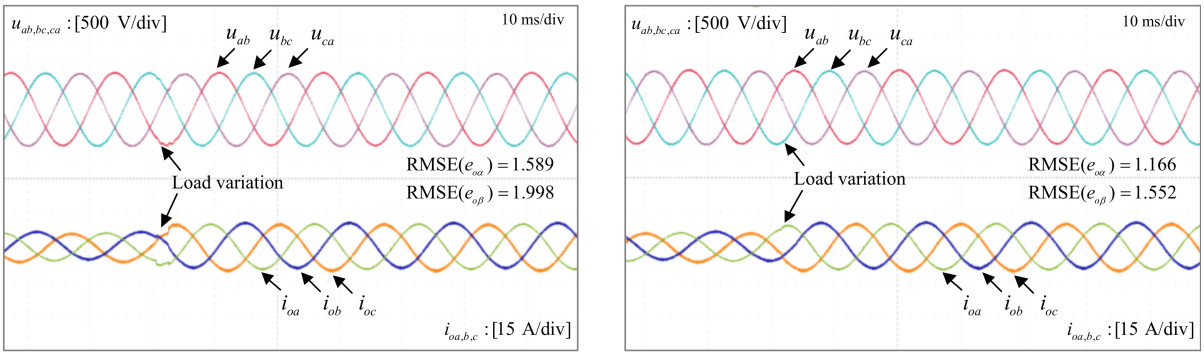

Figure 14. Experimental waveforms of inverter output voltages (u_{ab}, u_{bc}, u_{ca}) and currents (i_{oa}, i_{ob}, i_{oc}) under load variations: (**a**) quasi-PRC; (**b**) proposed TSMC.

5.2.2. Performance Verification of Proposed TSMC-Based Droop Control Method

To verify the effectiveness of the TSMC-based *P-U/Q-f* droop control method on power sharing, three cases are conducted. As for Case I, the inverters are assumed to have the same power capacity, so an equal load power sharing between the inverters should be achieved. In Case II, the difference of the line impedances is increased to illustrate the robustness of the proposed TSMC-based *P-U/Q-f* droop control method. In Case III, the power capacity of the inverter 1 is assumed to be twice of the one of the inverter 2, so the load power should be shared in the ratio of 2:1 between the inverter1 and the inverter 2. For each case, the conventional *P-U/Q-f* droop control method in [11], the PI-based *P-U/Q-f* droop control method in [15] and the proposed TSMC-based *P-U/Q-f* droop control method in this study are compared.

- Case I: Equal load power sharing with line impedance ratio of 2:1

In this case, the line impedance of 2 Ω for the inverter 1 and the one of 1 Ω for the inverter 2 are used to highlight the superiority of the proposed method. The rated powers of the two inverters are set to be the same. As can be seen from Figure 15a, affected by the difference of line impedances, the active powers of the two inverters can be hardly shared with the conventional *P-U/Q-f* droop control, and the power sharing error increases with the occurrence of load variations. By the same examined condition, the PI-based *P-U/Q-f* droop control method is adopted. As can be seen from Figure 15b, the active power sharing performance can be improved. However, the dynamic performance is degraded due to the proportional-integral behavior added on the proportional droop controller, and an active power sharing error exists during the transient state. When the TSMC-based droop control method is employed, as can be seen from Figure 15c, the dynamic performance can be improved, and excellent power sharing performance can be achieved during both the transient and steady states with less sensibility to load changes and line impedance.

- Case II: Equal load power sharing with line impedance ratio of 3:1

In this case, the line impedance of 3 Ω for the inverter 1 and the one of 1 Ω for the inverter 2 are used to illustrate the insensibility of the proposed method to line impedance. As can be seen from Figure 16a, when the conventional *P-U/Q-f* droop control method is adopted, the increasing of the line impedance difference results in a larger active power sharing error. As the load increases, the power sharing error will become larger, which means one of the inverters may be overloaded and the safety of the system is threatened. Figure 16b shows that when the PI-based *P-U/Q-f* droop control method is adopted, the line impedance has little effect on the power sharing at the steady state, but the dynamic response at load changes is affected. By comparing Figures 15b and 16b, one can notice that the increasing of the line impedance difference increases the active power sharing error during the transient state. Figure 16c shows that although the line impedances of the

inverter 1 and the inverter 2 differ a lot from each other, the TSMC-based *P-U/Q-f* droop control method still can achieve good control performance in both steady-state power sharing and transient response. Therefore, the proposed TSMC scheme shows a good robustness against uncertain changes and line impedances.

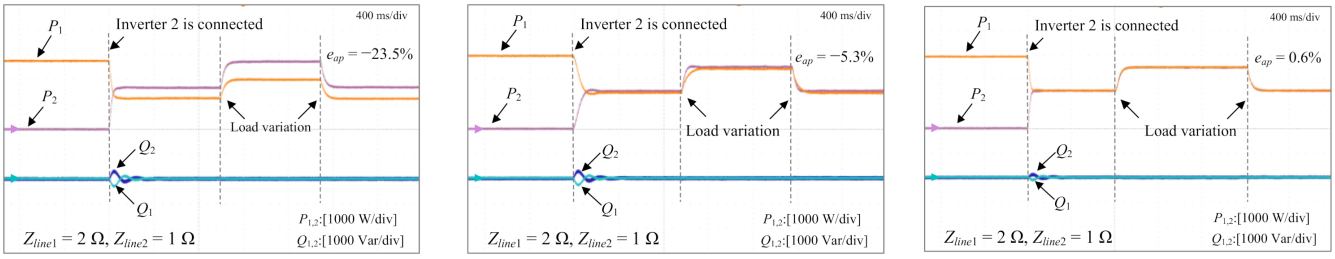

Figure 15. Experimental results of power responses with line impedance ratio of 2:1: (**a**) power sharing performance via conventional *P-U/Q-f* droop control method; (**b**) power sharing performance via PI-based *P-U/Q-f* droop control method; (**c**) power sharing performance via proposed TSMC-based *P-U/Q-f* droop control method.

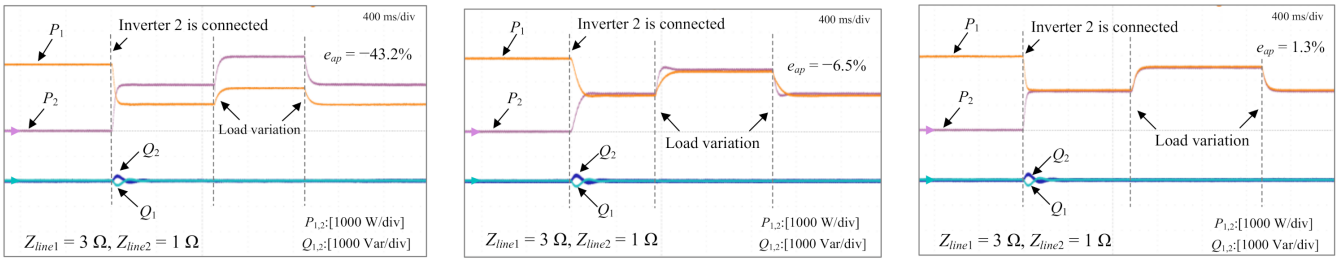

Figure 16. Experimental results of power responses with line impedance ratio of 3:1: (**a**) power sharing performance via conventional *P-U/Q-f* droop control method; (**b**) power sharing performance via PI-based *P-U/Q-f* droop control method; (**c**) power sharing performance via proposed TSMC-based *P-U/Q-f* droop control method.

- Case III: Power sharing with different inverter capacity

This case aims to examine the power sharing performance of the three control methods when the parallel inverters have different capacity. In order to compare the property of each method, a line impedance of 2 Ω is used for each inverter. Since the power capacity of the inverter 1 is assumed to be twice the one of the inverter 2, the output power of the two inverters should be allocated in the ratio of 2:1. As can be seen from Figure 17a, the conventional *P-U/Q-f* droop method cannot guarantee the desired proportion for load power sharing due to the influence of the line impedance. Moreover, Figure 17b shows that the PI-based *P-U/Q-f* droop control method can improve the power proportional sharing precision, but some sharing deviation still exists; the dynamic performance during the inverter connection and load changes needs to be improved. As can be seen from Figure 17c, when the TSMC-based *P-U/Q-f* droop control method is applied, the load power can be shared by the parallel inverters according to their rated capacities. Obviously, the proposed TSMC-based *P-U/Q-f* droop control method shows better power proportional sharing performance, and the corresponding dynamic response is better than the one of the PI-based *P-U/Q-f* droop control method and the conventional *P-U/Q-f* droop control method.

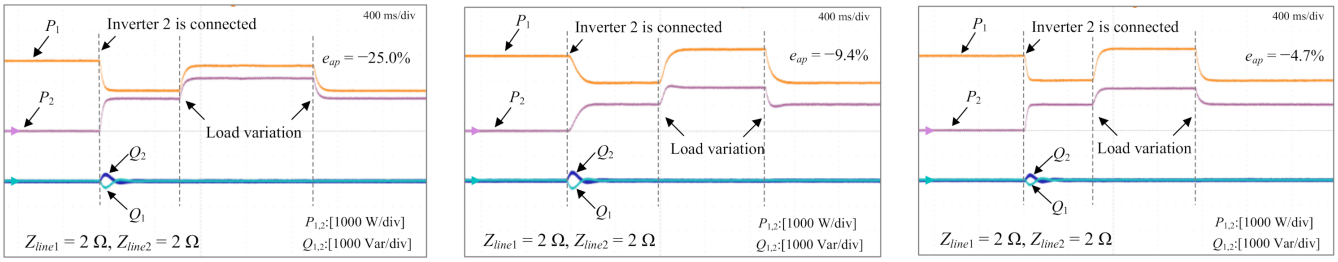

Figure 17. Experimental results of power responses as power capacity ratio of inverter 1 and inverter 2 to be 2:1: (**a**)power sharing performance via conventional *P-U/Q-f* droop control method; (**b**) power sharing performance via PI-based *P-U/Q-f* droop control method; (**c**) power sharing performance via proposed TSMC-based *P-U/Q-f* droop control method.

In order to verify the superiority of the proposed TSMC-based *P-U/Q-f* droop control method on voltage stabilization, a load change of 2 kW is conducted. First, the voltage stabilization with the conventional *P-U/Q-f* droop control method is examined, and the corresponding experimental results are depicted in Figure 18a. As can be seen from Figure 18a, the steady-state voltage amplitude (*E*) of the PCC before the load change is 308.1 V, deviating from the rated value (311 V) by about −0.93%. Then, after the load change, the steady-state voltage amplitude becomes 302.1 V and the corresponding amplitude deviating is −2.86%. Moreover, the amplitude variation of the PCC voltage under the load change can be further derived as −1.95%. As can be seen from Figure 18b,c, both the PI-based *P-U/Q-f* droop control method and the proposed TSMC-based *P-U/Q-f* droop control method can reduce the voltage deviation caused by the *P-U/Q-f* droop control and the line impedance. The amplitude deviating before and after the load change can be reduced to 0.61% and 0.19% by the PI-based *P-U / Q-f* droop method. In addition, the amplitude variation of the PCC voltage under the load change is reduced to −0.42%. When the proposed TSMC-based *P-U/Q-f* droop control method is adopted, the PCC voltage amplitudes are respectively restored to 311.5 V and 310.8 V before and after the load change, as shown in Figure 18c. The corresponding amplitude deviating are reduced to 0.16% and −0.06%, respectively. Furthermore, the amplitude variation of the PCC voltage under the load change can be further reduced to −0.23%. According to the analyses mentioned above, both the power sharing performance and the PCC voltage quality can be improved by the proposed TSMC-based *P-U/Q-f* droop control method.

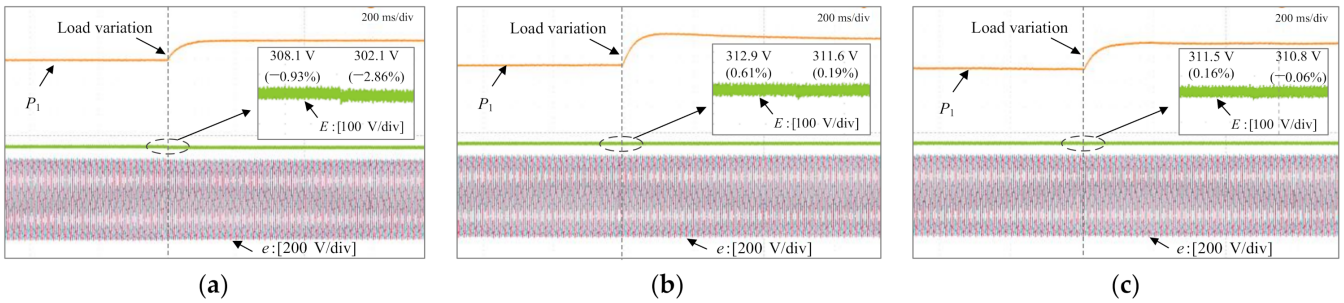

Figure 18. Experimental results of PCC voltage under load variations: (**a**) PCC voltage via conventional *P-U/Q-f* droop control method; (**b**) PCC voltage via PI-based *P-U/Q-f* droop control method; (**c**) PCC voltage via proposed TSMC-based *P-U/Q-f* droop control method.

According to the definition of the power allocation error (e_{ap}) in (39), the power sharing control performance can be represented by the value of the power allocation error (e_{ap}) between the parallel inverters, which is expected to be small. The corresponding evaluation results are summarized in Table 4. As can be seen from Table 4, with the proposed TSMC-based *P-U/Q-f* droop control method, the power allocation error (e_{ap}) can be reduced by 97.4% in comparison with the conventional droop control method in [11]

and 88.7% in comparison with the PI-based droop control method in [15] for the equal power sharing case (Case I). Moreover, a more extreme case (Case II) can further illustrate the superiorities of the proposed method. In addition, when the parallel inverters have different capacity (Case III), an 81.2% improvement for the conventional droop control method and a 50.0% improvement for the PI-based droop control method can be achieved by the proposed method. Therefore, the proposed TSMC scheme has a higher control precision. Simultaneously, compared with the conventional droop control method in [11] and the PI-based droop control method in [15], the deviation rate of the PCC voltage can be reduced by 82.8% and 73.8%, respectively. Moreover, the corresponding PCC voltage variation improvements under load change are 88.2% and 45.2%. Therefore, the proposed method not only can achieve good power sharing performance, but also improve the PCC voltage quality.

Table 4. Performance comparisons of different control methods.

Test Conditions	Conventional Droop Control Method [11]	PI-based Droop Control Method [15]	Proposed TSMC-based Droop Control Method
Power allocation error (e_{ap}) (Case I)	−23.5%	−5.3%	0.6%
Power allocation error (e_{ap}) (Case II)	−43.2%	−6.5%	1.3%
Power allocation error (e_{ap}) (Case III)	−25.0%	−9.4%	−4.7%
PCC voltage deviation rate	−0.93%/−2.86%	0.61%/0.19%	0.16%/−0.06%
PCC voltage variation rate	−1.95%	−0.42%	−0.23%

6. Conclusions

In this study, a total-sliding-mode-control (TSMC)-based *P-U/Q-f* droop control structure has been successfully designed for the parallel-connected inverter system to achieve the objectives of accurate power sharing and high voltage quality. Owing to the TSMC-based frameworks for both the inner voltage loop and droop control loop, the system dynamic performance can be improved, and the active power allocation accuracy during both the transient and steady states can be effectively increased. The power allocation error (e_{ap}) can be reduced by more than 81.2% and 50% in comparison with the conventional droop control method in [11] and the proportional-integral (PI)-based droop control method in [15], respectively. Simultaneously, the voltage amplitude deviation of the point of common coupling (PCC) can be greatly alleviated by the feedback structures. The PCC voltage deviation rate can be reduced to 0.16% and −0.06% before and after load change. Experimental results also show that when the PI-based *P-U/Q-f* droop controller in [15] is adopted, the active power sharing performance during the transient state is easily influenced by the line impedance, but the proposed TSMC-based scheme exhibits a good robustness against line impedance. Therefore, this new control structure endows the system with the advantages of accurate power sharing during both the transient and steady states, high voltage quality, superior dynamic response and strong robustness. The parameter influences on the system stability and the dynamic response have been investigated via the small-signal stability analyses of the TSMC-based droop-controlled system. The proposed TSMC-based droop controller can share the active power among DGs based on the ratios of their capacities. However, an economic operation of the system has not been covered in this study. Because the minimization of generation costs is usually more desirable from the perspective of the economic operation, it is worthy to be investigated in the future work. Due to the requirement of the PCC voltage in this study, it will limit the applications of the proposed control framework without communications. With the development of the information technology, various communication-based methods have been applied to MGs, the problems of communication delay and data packet loss will be studied in the future work.

Author Contributions: Conceptualization, Q.-Q.Z.; methodology, Q.-Q.Z. and R.-J.W.; software, Q.-Q.Z.; formal analysis, Q.-Q.Z.; writing—original draft preparation, Q.-Q.Z.; writing—review and editing, Q.-Q.Z. and R.-J.W.; project administration, R.-J.W.; funding acquisition, R.-J.W. All authors have read and agreed to the published version of the manuscript.

Funding: This research was funded in part by [Ministry of Science and Technology of Taiwan] grant number [108-2221-E-011-080-MY3].

Institutional Review Board Statement: Not applicable.

Informed Consent Statement: Not applicable.

Data Availability Statement: Not applicable.

Conflicts of Interest: The authors declare no conflict of interest.

Nomenclature

Abbreviations	
DGs	Distributed generations
DSP	Digital signal processor
ESR	Equivalent series resistance
EMU	Energy management unit
FPGA	Field programmable gate array
MG	Micro-grid
MPC	Model predictive control
PI	Proportional-integral
PID	Proportion-integration-differentiation
PTL	Power transmission lines
PCC	Point of common coupling
PWM	Pulse-width-modulation
PRC	Proportional-resonant controller
RMSE	Root-mean-squared error
SAPFs	Shunt active power filters
SVPWM	Space-vector PWM
TSMC	Total sliding-mode control
VOT	Vector operation technique
VSI	Voltage source inverter
P-f	Active power-frequency
P-U	Active power-voltage
Q-f	Reactive power-frequency
Q-U	Reactive power-voltage
Variables and parameters	
P_n	Output active power
Q_n	Output reactive power
U_n	Voltage amplitude of DGn
ω_n	Angle frequency of DGn
E	Voltage amplitude of PCC
P_n^m	Measured active power
Q_n^m	Measured reactive power
δ_n	Phase angle of DGn
δ_c	Phase angle of PCC
U_{dc}	DC-link voltage of DG
$u_{o\alpha}$, $u_{o\beta}$	Capacitance-voltage components of α and β axis
$i_{o\alpha}$, $i_{o\beta}$	Output currents in α and β axis
$u_{\mathrm{con}\alpha}$, $u_{\mathrm{con}\beta}$	Control efforts of α and β axis
S_{pn}	Total sliding surface for power control loop
$\boldsymbol{S}$	Total sliding surface for voltage control loop

U_0	Rated voltage amplitude
ω_0	Rated angular frequency
P_n^*	Rated active power
Q_n^*	Rated reactive power
u_α^*,u_β^*	Voltage commands generated by droop controller
$u_{o\alpha}^*$,$u_{o\beta}^*$	Capacitance voltage references of α and β axis
ω_f	Cutoff frequency of low-pass filter for power
m_n	Droop coefficient of *P-U*
n_n	Droop coefficient of *Q-f*
k_e	Proportional factor of U_0-*E* feedback loop
c_1, K, c_2	Control parameters of TSMC-based droop controller
k_1, k_2, ρ, c_3	Control parameters of TSMC-based voltage controller
K_{PWM}	PWM gain
R_v	Virtual resistance of DG*n*
L_v	Virtual inductance
R_n	Line resistance
L_f	Filter inductor
C_f	Filter capacitor
r_f	ESR of filter inductor

References

1. Afshar, Z.; Mollayousefi, M.; Bathaee, S.M.T.; Bina, M.T.; Gharehpetian, G.B. A novel accurate power sharing method versus droop control in autonomous microgrids with critical loads. *IEEE Access* **2019**, *7*, 89466–89474. [CrossRef]
2. Zhang, W.; Wang, W.; Liu, H.; Xu, D. A disturbance rejection control strategy for droop-controlled inverter based on super-twisting algorithm. *IEEE Access* **2019**, *7*, 27037–27046. [CrossRef]
3. Hossain, M.A.; Pota, H.R.; Issa, W.; Hossain, M.J. Overview of AC microgrid controls with inverter-interfaced generations. *Energies* **2017**, *10*, 1300. [CrossRef]
4. Yu, K.; Ai, Q.; Wang, S.; Ni, J.; Lv, T. Analysis and optimization of droop controller for microgrid system based on small-signal dynamic model. *IEEE Trans. Smart Grid* **2015**, *7*, 695–705. [CrossRef]
5. Wang, K.; Yuan, X.; Geng, Y.; Wu, X. A practical structure and control for reactive power sharing in microgrid. *IEEE Trans. Smart Grid* **2019**, *10*, 1880–1888. [CrossRef]
6. Chen, T.; Abdel-Rahim, O.; Peng, F.; Wang, H. An improved finite control set-MPC-based power sharing control strategy for islanded AC microgrids. *IEEE Access* **2020**, *8*, 52676–52686. [CrossRef]
7. Yan, X.; Cui, Y.; Cui, S. Control method of parallel inverters with self-synchronizing characteristics in distributed microgrid. *Energies* **2019**, *12*, 3871. [CrossRef]
8. He, J.; Du, L.; Liang, B.; Li, Y.; Wang, C. Coupled-virtual-impedance control for AC/DC hybrid microgrid power electronic interlinking unit with dual converters. *IEEE Trans. Smart Grid* **2019**, *10*, 3387–3400. [CrossRef]
9. Tang, X.; Hu, X.; Li, N.; Deng, W.; Zhang, G. A novel frequency and voltage control method for islanded microgrid based on multienergy storages. *IEEE Trans. Smart Grid* **2016**, *7*, 410–419. [CrossRef]
10. Pogaku, N.; Prodanovic, M.; Green, T.C. Modeling, analysis and testing of autonomous operation of an inverter-based microgrid. *IEEE Trans. Power Electron.* **2007**, *22*, 613–625. [CrossRef]
11. Guerrero, J.M.; de Vicuna, L.G.; Matas, J.; Castilla, M.; Miret, J. Output impedance design of parallel-connected UPS inverters with wireless load sharing control. *IEEE Trans. Ind. Electron.* **2005**, *52*, 1126–1135. [CrossRef]
12. Wang, X.F.; Li, Y.W.; Blaabjerg, F.; Zoh, P.C. Virtual-impedance-based control for voltage-source and current-source converters. *IEEE Trans. Power Electron.* **2015**, *30*, 7019–7037. [CrossRef]
13. Guan, Y.; Guerrero, J.M.; Zhao, X.; Vasquez, J.C.; Guo, X.Q. A new way of controlling parallel-connected inverters by using synchronous-reference-frame virtual impedance loop-part I: Control principle. *IEEE Trans. Power Electron.* **2016**, *31*, 4576–4593. [CrossRef]
14. Zhong, Q.C. Robust droop controller for accurate proportional load sharing among inverters operated in parallel. *IEEE Trans. Ind. Electron.* **2013**, *60*, 1281–1290. [CrossRef]
15. Wai, R.J.; Zhang, Q.Q.; Wang, Y. A novel voltage stabilization and power sharing control method based on virtual complex impedance for off-grid microgrid. *IEEE Trans. Power Electron.* **2019**, *34*, 1863–1880. [CrossRef]
16. Kahrobaeian, A.; Mohamed, Y.A.R.I. Networked-based hybrid distributed power-sharing and control for islanded microgrid systems. *IEEE Trans. Power Electron.* **2015**, *30*, 603–617. [CrossRef]
17. Mahmud, K.; Sahoo, A.K.; Ravishankar, J.; Dong, Z.Y. Coordinated multilayer control for energy management of grid-connected AC microgrids. *IEEE Trans. Ind. Appl.* **2019**, *55*, 7071–7081. [CrossRef]
18. Shan, Y.; Hu, J.; Liu, M.; Zhu, J.; Guerrero, J.M. Model predictive voltage and power control of islanded PV-battery microgrids with washout-filter-based power-sharing strategy. *IEEE Trans. Power Electron.* **2020**, *35*, 1227–1238. [CrossRef]

19. Zhu, Y.X.; Zhuo, F.; Shi, H.T. Accurate power sharing strategy for complex microgrid based on droop control method. In Proceedings of the 2013 IEEE ECCE Asia Downunder, Melbourne, Australia, 3–6 June 2013; pp. 344–350.
20. Wu, X.; Xu, Y.; He, J.; Wang, X.; Vasquez, J.C.; Guerrero, J.M. Pinning-based hierarchical and distributed cooperative control for AC microgrid clusters. *IEEE Trans. Power Electron.* **2020**, *35*, 9865–9885. [CrossRef]
21. Yazdanian, M.; Mehrizi-Sani, A. A washout filter-based power sharing. *IEEE Trans. Smart Grid* **2016**, *7*, 967–968. [CrossRef]
22. Ma, L.; Zhang, Y.F.; Yang, X.F.; Ding, S.H.; Dong, L.L. Quasi-continuous second-order sliding mode control of buck converter. *IEEE Access* **2018**, *6*, 17859–17867. [CrossRef]
23. Han, Y.; Ma, R.; Cui, J. Adaptive higher-order sliding mode control for islanding and grid-connected operation of a microgrid. *Energies* **2018**, *11*, 1459. [CrossRef]
24. Wang, Y.; Wai, R.J. Design of discrete-time backstepping sliding-mode control for LCL-type grid-connected inverter. *IEEE Access* **2020**, *8*, 95082–95098. [CrossRef]
25. Vadi, S.; Padmanaban, S.; Bayindir, R.; Blaabjerg, F.; Mihet-Popa, L. A review on optimization and control methods used to provide transient stability in microgrids. *Energies* **2019**, *12*, 3582. [CrossRef]
26. Wai, R.J. Development of intelligent position control system using optimal design technique. *IEEE Trans. Ind. Electron.* **2003**, *50*, 218–231.
27. Morales, J.; Vicuna, L.G.; Guzman, R.; Castilla, M.; Miret, J. Modeling and sliding mode control for three-phase active power filters using the vector operation technique. *IEEE Trans. Ind. Electron.* **2018**, *65*, 6828–6838. [CrossRef]
28. Guzman, R.; Vicuna, L.G.; Castilla, M.; Miret, J.; Hoz, J. Variable structure control for three-phase LCL-filtered inverters using a reduced converter model. *IEEE Trans. Ind. Electron.* **2018**, *65*, 5–15. [CrossRef]
29. Vieira, R.P.; Martins, L.T.; Massing, J.R.; Stefanello, M. Sliding mode controller in a multiloop framework for a grid-connected VSI with LCL filter. *IEEE Trans. Ind. Electron.* **2018**, *65*, 4714–4723. [CrossRef]
30. Mokhtar, M.; Marei, M.I.; EI-Sattar, A.A. An adaptive droop control scheme for DC microgrids integrating sliding mode voltage and current controlled boost converters. *IEEE Trans. Smart Grid* **2017**, *10*, 1685–1693. [CrossRef]
31. Altin, N.; Ozdemir, S.; Komurcugil, H.; Sefa, I. Sliding-mode control in natural frame with reduced number of sensors for three-phase grid-tied LCL-interfaced inverters. *IEEE Trans. Ind. Electron.* **2019**, *66*, 2903–2913. [CrossRef]
32. Delghavi, M.B.; Yazdani, A. Sliding-mode control of AC voltages and currents of dispatchable distributed energy resources in master-slave-organized inverter-based microgrids. *IEEE Trans. Smart Grid* **2019**, *10*, 980–991. [CrossRef]
33. Wang, Y.; Wai, R.J. Adaptive power decoupling strategy for single-phase grid-connected converter. *IEEE Trans. Ind. Appl.* **2019**, *55*, 4275–4285. [CrossRef]
34. Wai, R.J.; Lin, C.Y. Active low-frequency ripple control for clean-energy power-conditioning mechanism. *IEEE Trans. Ind. Electron.* **2010**, *57*, 3780–3792. [CrossRef]
35. Hosseinzadeh, M.; Yazdanpanah, M.J. Performance enhanced model reference adaptive control through switching non-quadratic Lyapunov functions. *Syst. Control. Lett.* **2015**, *76*, 47–55. [CrossRef]
36. Tao, G. Model reference adaptive control with L1+α tracking. *Int. J. Control.* **1996**, *64*, 859–870. [CrossRef]